Solution of population balance equations in applications with fine particles: mathematical modeling and numerical schemes

Tan Trung Nguyen, Frédérique Laurent, Rodney Fox, Marc Massot

Solution of population balance equations in applications with fine particles: mathematical modeling and numerical schemes

T. T. Nguyen[a,b], F. Laurent[a,b,*], R. O. Fox[a,b,c], M. Massot[a,b]

[a] *Laboratoire EM2C, CNRS, CentraleSupélec, Université Paris-Saclay, Grande Voie des Vignes, 92295 Châtenay-Malabry cedex, France*
[b] *Fédération de Mathématiques de l'Ecole Centrale Paris, FR CNRS 3487, France*
[c] *Department of Chemical and Biological Engineering, 2114 Sweeney Hall, Iowa State University, Ames, IA 50011-2230, USA*

Abstract

The accurate description and robust simulation, at relatively low cost, of global quantities (*e.g.* number density or volume fraction) as well as the size distribution of a population of fine particles in a carrier fluid is still a major challenge for many applications. For this purpose, two types of methods are investigated for solving the population balance equation with aggregation, continuous particle size change (growth and size reduction), and nucleation: the extended quadrature method of moments (EQMOM) based on the work of Yuan et al. (J. Aerosol Sci., 51:1–23, 2012) and a hybrid method (TSM) between the sectional and moment methods, considering two moments per section based on the work of Laurent et al. (Commun. Comput. Phys., accepted, 2016, https://hal.archives-ouvertes.fr/hal-01169730). For both methods, the closure employs a continuous reconstruction of the number density function of the particles from its moments, thus allowing evaluation of all the unclosed terms in the moment equations, including the negative flux due to the disappearance of particles. Robust and accurate numerical methods are developed, ensuring the realizability of the moments. The robustness is ensured with efficient and tractable algorithms despite the numerous couplings and various algebraic constraints thanks to a tailored overall strategy. EQMOM and TSM are compared to the classical sectional method for various test cases, showing their ability to describe accurately the fine-particle population with a much lower number of variables. These results demonstrate the efficiency of the modeling and numerical choices, and their potential for the simulation of real-world applications.

Keywords: aerosol, population balance equation, quadrature-based moment method, sectional method, hybrid method

1. Introduction

The evolution of a population of fine, that is non-inertial, particles in a carrier fluid can be described by a population balance equation (PBE) [1, 2, 3, 4, 5, 6, 7, 8, 9, 10]. There are many

*Corresponding author
Email addresses: tan-trung.nguyen@centralesupelec.fr (T. T. Nguyen), frederique.laurent@centralesupelec.fr (F. Laurent), rofox@iastate.edu (R. O. Fox), marc.massot@centralesupelec.fr (M. Massot)

potential applications such as soot modeling, aerosol technology, nanoparticle synthesis, microbubbles, reactive precipitation, and coal combustion (see [5] and references therein). The PBE is a transport equation for the number density function (NDF) of the particles. The NDF depends on time, spatial location and the internal coordinates, which can include, for example, volume, surface area or chemical composition. The mathematical form of a typical PBE includes spatial transport (*e.g.* convection and diffusion), derivative source terms for continuous particle size change (*e.g.* oxidation/dissolution and surface growth), integral terms (*e.g.* aggregation and breakage), and Dirac-delta-function source terms describing the formation of particles (*e.g.* nucleation). Moreover, it is usually not only important to predict the evolution of global quantities of the particle population, but also to have some information on the NDF. For example, when considering soot, the total produced mass or volume fraction, as well as the size-dependent NDF represent essential elements in present and future emission regulations. But since the evolution of the NDF is usually coupled with the resolution of the Navier-Stokes equation for the carrier fluid [10], the cost of its resolution has to be reasonable so that the global simulation will be affordable. We therefore seek a robust method able to describe accurately some global quantities of the particle population, but also able to give a good idea of the shape of the NDF, at a reasonable cost.

In this work, only size is considered as the internal variable. Moreover, even if the geometry of fine particles can be complex, we assume that only one variable, *e.g.* volume v, is needed to describe it, eventually taking into account the more complex shape of large particles compared to smaller ones through a fractal dimension depending on size. This work thus represents a first step before considering more complex models that add another internal coordinate variable. Different methods are available in the literature to solve the PBE. The Monte-Carlo method [2] is usually too costly to be coupled with a flow solver, especially when considering particle interactions like aggregation. We therefore focus on deterministic methods.

With one internal variable, deterministic methods can be based on a discretization along the size variable. Equations are written for the total number density or the total mass density of the particles inside each interval of the size-discretization. These intervals are called sections in what follows, in reference to the sectional methods, which fall in this category. A large literature is devoted to this type of method, especially for the resolution of the aggregation and/or breakage PBE (see *e.g.* [11, 12, 13] and references therein). Among them are the fixed-pivot [11] and the cell-average [14] techniques, which consider that the particle population of one section is represented by only one size (pivot size), the new particles after collision or breakup being distributed over the sections in such a way that the discrete equations are consistent with the global number and mass (they are said to be "moment preserving"). These methods have been combined with the method of characteristics to treat the growth terms in order to solve the PBE with simultaneous nucleation, growth and aggregation [15]. Some other methods are based on a "conservative form" of the PBE for the mass density function [16, 17]: a conservative finite-volume method developed for aggregation and breakup [16, 17] and extended to growth and nucleation [18], or some moment-preserving methods [19]. These methods have been shown to be convergent when considering only aggregation or breakup, with first-order accuracy for the finite-volume methods [16, 17] and second-order accuracy for the fixed-pivot and cell-average techniques [20, 21, 22]. But a large number of sections is always used and the ability of these methods to describe adequately the NDF with a small number of sections has not been fully explored, especially for the complete problem with nucleation and growth. Moreover, such methods have never been reported for cases where the particle size is decreasing through a continuous process.

A different kind of method, the only one that will be called sectional here (even if some of the

previous ones are also called sectional in the literature), is based on a closure through a continuous reconstruction of the NDF inside each section. This reconstruction can be constant [23, 24, 25] or affine [26, 27]. When considering sprays, sectional methods are also called "Eulerian multi-fluid methods" [24], and they are developed after reduction of the internal variables to only size thanks to velocity moments and a mono-kinetic closure. The corresponding model is a finite-volume method. It was shown to be first-order accurate in the pure-evaporation case [28] and exhibited first-order numerical accuracy for the investigated cases, taking into account the collisions (coalescence) [29]. Moreover, in this approach, an affine reconstruction of MUSCL type was tested in the pure-evaporation case. However, if its order of accuracy is higher, the effective accuracy is not much improved compared to the first-order method, except with a large number of sections. Then, as with other discretized methods, sectional methods lead to an accurate prediction of the NDF with a large enough number of sections. However, for many applications, physical transport must also be considered, as well as coupling with the carrier fluid. This can be done thanks to the use of an operator-splitting method (see *e.g.* [30]), but if a large number of sections has to be considered, the computational cost can be prohibitive, since one has to transport at least one variable per section.

In contrast, moment methods do not use a direct resolution of the NDF, but rather transport a finite set of its moments, usually the first few integer order ones. Since they are the moments of a non-negative NDF (or, more rigorously, a positive measure), this moment set belongs to a space strictly included in $\mathbb{R}_+^N$, where N is the number of moments [31, 32, 33]. This space is called the moment space. The NDF cannot be recovered from this finite moment set: there is an infinite number of possibilities in non-degenerate cases, *i.e.* when the moment set is in the interior of moment space, whereas a unique sum of weighted Dirac delta functions is possible for the degenerate cases, *i.e.* for the boundary of moment space. One can remark that the degenerate case can appear in problems of interest due to nucleation of fine particles just as they begin to aggregate. Most importantly, moment methods give access to some important properties of the NDF.

For moment methods, two major issues arise. The first is closure of the moment equations due to the nonlinear source terms in the PBE. This includes the negative flux due to the disappearance of particles when continuous size reduction is considered (*e.g.* oxidation or evaporation), which requires a point-wise evaluation of the NDF [34]. Two kinds of closures are used in the literature: (i) a functional dependence of the unclosed terms (usually expressed through some fractional moments) is provided using the moment set; (ii) a NDF, or its corresponding measure, is reconstructed from the moment set, allowing evaluation of all the unclosed terms. In the first category, one finds the interpolative closure (MOMIC) [35, 36] widely used in the soot community and extended to the bivariate case [37]. MOMIC is based on an interpolation along the order of the moments. However, this kind of method does not allow one to deal with the disappearance fluxes, except for the hybrid method of moments (HMOM) [38], which is a combination of MOMIC and DQMOM described below and was developed for a bivariate case. Moreover, these methods do not guarantee that the closure can correspond to any NDF. This is why a second way to close the moment equations has been developed using quadrature-based moment methods (QBMM) [39, 1, 2].

Because the internal variable (size) is assumed to live in the semi-infinite space $[0, \infty)$, the problem of NDF reconstruction from a finite set of moments is known as the truncated Stieljes moment problem [31, 33][1]. Among these reconstructions, a sum of weighted Dirac delta functions

[1] It is the truncated Hausdorff moment problem if the internal variable lives in a compact support, and the Hamburger problem if it lives on the real line.

can be used, leading to the widely employed quadrature method of moments (QMOM) [40]. This reconstruction for an even set of integer moments $(m_0, m_1, \ldots, m_{2N-1})$ is the lower principal representation, *i.e.* the corresponding moment m_{2N} is minimal. In its variant, the direct quadrature method of moments (DQMOM) [41], the equations are directly written for the weights and abscissas of the reconstruction, leading however to some shortcomings related to the conservation of moments. Although these methods have the advantage of being applicable to multivariate cases (directly for DQMOM or using the conditional quadrature method of moments (CQMOM) [42]), they still cannot deal with disappearance fluxes [43]. A continuous NDF reconstruction must be considered for this purpose.

One such reconstruction is entropy maximization, which is well defined for the truncated Hausdorff moment problem [44, 45], and an algorithm is available to reproduce any moment set with reasonable accuracy [46]. Entropy maximization has been used for sprays [34, 47, 46]. However, when considering the truncated Stieljes moment problem, it fails to reproduce some moment sets [48]. Some other types of reconstructions have been proposed (see [49] and references therein), but either with a too low number of moments in such a way that multi-nodal distributions, which often appear in the problems of interest here, cannot be described, or with almost always some negative values for the reconstructed NDF, thus leading to potential instability issues for their numerical resolution. For the truncated Hausdorff moment problem, a nonnegative reconstruction was developed using a superposition of kernel density functions (KDF) (kernel density element method, KDEM) [50]. However, KDEM only guarantees that some of the low-order moments are exactly preserved [49]. First for the truncated Hamburger moment problem [51], and then for the truncated Hausdorff and Stieljes moment problems [49, 52], a nonnegative reconstruction was developed using QBMM, allowing to exactly preserve all the moments except sometimes the last one. The reconstructed NDF is then a sum of nonnegative weighted KDF, able to converge to the Dirac delta function, even if this transition is not yet numerically effective in the proposed algorithms. The QBMM corresponding to this closure is called the extended quadrature method of moments (EQMOM) and was, for example, applied to soots in [53].

The second major issue associated with moment methods is realizability: the moments must remain in moment space, which is a convex space [31, 32, 33]. This issue is not always considered, especially when the first type of closure is used, thus leading to unphysical results (*e.g.* invalid moment sets). Indeed, even if the closure itself ensures the realizability at the continuous level, the classical schemes for high-order transport in physical space can lead to an invalid moment set [54, 55, 56], as well as for transport in phase space, especially when considering continuous particle size reduction [34] and/or the transition between a Dirac distribution (due to the nucleation) and a smooth distribution (due to the aggregation/coagulation). To circumvent this issue, some authors resort to moment correction algorithms [57, 54] based on a necessary but not sufficient condition for realizability [31] in order to obtain a valid moment set. The cost of the method then increases and the correction spoils the overall accuracy. This is why, in this paper, the developed schemes directly preserve the realizability of the moment set [34, 47, 2].

In recent years, a third type of method, which is a hybrid method between the sectional and moment methods, has been developed in the context of sprays [29, 58, 59, 34, 47, 46]. This method uses more than one moment per section and then a more accurate reconstruction on the section from these moments. If the realizability issue has also to be considered, contrary to moment methods, its complexity is often low since only a few moments are considered (typically two or eventually four). Among these hybrid methods, the two–size moment (TSM) method has been shown to be very accurate for evaporation (*i.e.* size reduction), as well as for coalescence (*i.e.* collisions) thanks

to a second-order accurate reconstruction of the NDF from the moments in the section [29], leading also to a good representation of the NDF with a small number of sections. Thus, TSM is a useful method for the fine-particle applications of interest here.

In this paper, we focus on both EQMOM and TSM in the context where the following physical phenomena are considered (*i.e.* all types of processes except spatial transport): nucleation, aggregation, continuous growth and size reduction. Robust reconstruction algorithms are provided for each method, accounting for boundary detection of moment space in the case of EQMOM. Moreover, since operator time-splitting techniques will be used for the complete problem, realizable schemes are developed for each operator separately. The remainder of the paper is organized as follows. Section 2 is dedicated to the description of EQMOM and TSM: the closures are given, as well as efficient algorithms to compute them. Then, realizable numerical schemes are provided and the methods are compared to the classical sectional method when considering particle size reduction and growth (Sec. 3), aggregation (Sec. 4), and a combination of nucleation, aggregation and size reduction (Sec. 5). Conclusions are drawn in Sec. 6.

2. Mathematical Model

The hybrid and quadrature-based moment methods that will be used in this work are derived from the spatially homogeneous and mono-variate PBE, considering nucleation, aggregation and continuous particle size change. For the hybrid method, TSM is used, with a reconstruction in the volume or radius variable. For the QBMM, EQMOM is used with a gamma or a log-normal KDF. The PBE is first recalled and the equations for the moments of the NDF on an arbitrary interval are given. To close the equations, a non-negative NDF is reconstructed and the details of this reconstruction are provided for each method. Moreover, the moment space is described in each case.

2.1. Population balance equation (PBE)

Let us consider the volume v as the only internal variable. In the case of spatial homogeneity, the NDF $f(t,v)$ is only a function of time t and v and the PBE reads

$$\frac{\partial f(t,v)}{\partial t} = S_{\text{nuc}} + S_{\text{agg}} + S_{\text{gro}} + S_{\text{red}} \tag{1}$$

with $t \geq 0$ and $v \geq 0$. The source terms corresponding to nucleation S_{nuc}, aggregation S_{agg}, surface growth S_{gro}, and continuous size reduction S_{red} are given, respectively, by

$$S_{\text{nuc}} = j(t)\,\delta(v - V_{\text{nuc}}) \tag{2a}$$

$$S_{\text{agg}} = \frac{1}{2}\int_0^v \beta(t, v-v', v')\, f(t, v-v')\, f(t,v')\,\mathrm{d}v' - f(t,v)\int_0^\infty \beta(t,v,v')\, f(t,v')\,\mathrm{d}v' \tag{2b}$$

$$S_{\text{gro}} = \partial_v[\mathcal{R}_{\text{gro}}(t,v)\, f(t,v)] \qquad S_{\text{red}} = \partial_v[\mathcal{R}_{\text{red}}(t,v)\, f(t,v)] \tag{2c}$$

where the nuclei volume V_{nuc} is constant and $j(t)$ is the nucleation rate [60, 37, 38]. Moreover, $\beta(t,v,v')$ is the aggregation kernel, $\mathcal{R}_{\text{gro}}(t,v) \geq 0$ the surface growth rate, and $\mathcal{R}_{\text{red}}(t,v) \leq 0$ the rate of size reduction. From the literature there are several types of aggregation kernels such as sum, product or Brownian [49, 2]. Only the sum and Brownian kernels will be considered in what follows, the first for verification purposes since some analytical solutions are available, and the second for a more physical dependence on the size. Time-dependent kernels will not be considered.

The drift terms (2c) depend on the particle geometry as well as on the size change process. They represent the rate $\frac{\mathrm{d}v}{\mathrm{d}t}$ of change of the particle volume. In the case of particle size reduction, $\mathcal{R}_{\mathrm{red}}(t,v)$ is usually proportional to the particle surface. For a spherical particle, this leads to

$$\mathcal{R}_{\mathrm{red}}(t,v) = -c_{\mathrm{red}}(t)\, v^{2/3} \mathbb{1}_{\mathbb{R}_+}(v) \leq 0 \tag{3}$$

where $c_{\mathrm{red}}(t)$ depends only on time. While the small particles are nearly spherical, this is usually not the case of the larger ones. A fractal dimension depending on the volume can be used in order to express the surface area as a function of the volume. However, this is not done here: the methods will be evaluated with simple models in the framework of this paper. For surface growth, we consider diffusion-controlled growth [40], meaning that the radius r of the particle increases proportionally to $1/r$. For spherical particles, this leads to the following volume change rate (see Appendix A):

$$\mathcal{R}_{\mathrm{gro}}(t,v) = c_{\mathrm{gro}}(t)\, v^{1/3} \geq 0 \tag{4}$$

where $c_{\mathrm{gro}}(t)$ is independent of the volume. In what follows, the variable $v^{1/3}$, which is proportional to the radius when considering spherical particles, will be denoted r and used as the variable of interest in our example results.

A typical solution of the PBE in fine-particle applications starts with a Dirac delta function, due to nucleation [4]. Then, the aggregation causes particles of larger sizes to appear, whereas the drift terms make the sizes of all particles evolve continuously. So, from monodisperse, the distribution becomes polydisperse, with eventually a short period of time where there are only a few sizes. One then has to deal with all these cases with our approximate models based on QBMM and hybrid methods.

2.2. Moment equations and related issues

Let us consider the interval $]V_{\min}, V_{\max}[$, which will be the semi-infinite space $[0,\infty)$ for QBMM or a section for the hybrid method. Consider the moment of order k of the NDF on this interval: with $k \in \{0,1,\ldots,N\}$. Multiplying the PBE (1) by v^k and integrating over the support, we obtain the following ordinary differential equations (ODE) for m_k:

$$\frac{dm_k}{dt} = \langle S_{\mathrm{nuc}}, v^k\rangle + \langle S_{\mathrm{agg}}, v^k\rangle + \langle S_{\mathrm{gro}}, v^k\rangle + \langle S_{\mathrm{red}}, v^k\rangle \tag{5}$$

where

$$\langle S_{\mathrm{nuc}}, v^k\rangle = V_{\mathrm{nuc}}^k\, j(t)\, \mathbb{1}_{]V_{\min},V_{\max}[}(V_{\mathrm{nuc}}) \tag{6a}$$

$$\langle S_{\mathrm{agg}}, v^k\rangle = \frac{1}{2}\iint_{\Omega} (v+v')^k \beta(t,v,v') f(t,v)\, f(t,v') \mathrm{d}v\mathrm{d}v' - \int_{V_{\min}}^{V_{\max}} v^k f(t,v) \int_0^{\infty} \beta(t,v,v')\, f(t,v') \mathrm{d}v'\mathrm{d}v \tag{6b}$$

$$\langle S_{\mathrm{gro}}, v^k\rangle = V_{\max}^k \mathcal{R}_{\mathrm{gro}}(t,V_{\max}) f(t,V_{\max}) - V_{\min}^k \mathcal{R}_{\mathrm{gro}}(t,V_{\min}) f(t,V_{\min}) - k\int_{V_{\min}}^{V_{\max}} v^{k-1} \mathcal{R}_{\mathrm{gro}}(t,v) f(t,v) \mathrm{d}v \tag{6c}$$

$$\langle S_{\mathrm{red}}, v^k\rangle = V_{\max}^k \mathcal{R}_{\mathrm{red}}(t,V_{\max}) f(t,V_{\max}) - V_{\min}^k \mathcal{R}_{\mathrm{red}}(t,V_{\min}) f(t,V_{\min}) - k\int_{V_{\min}}^{V_{\max}} v^{k-1} \mathcal{R}_{\mathrm{red}}(t,v) f(t,v) \mathrm{d}v \tag{6d}$$

and $\Omega = \{(v, v') > 0 \,/\, V_{\min} \leq v + v' \leq V_{\max}\}$. This set of ODEs for $k \in \{0, 1, \ldots, N\}$ is unclosed since the NDF is unknown. Here, in order to be sure that the source terms are physical, the NDF will be reconstructed from its moments,. This reconstruction will have to be well defined for all the physically possible cases, including monodisperse or discrete polydisperse cases, and will have to give a representative value of the NDF at each bound of the interval in cases where this bound is not infinite. Finally, the set of moments lives in a convex space, which is described in the next subsection, and the numerical scheme will have to guarantee that the computed moment set will stay in this space.

Let us remark that the volume variable is used for the NDF as well as for the moment definition. However, for size reduction, the variable $r = v^{1/3}$ is also interesting since it decreases in an affine way. This is why integer moments for this variable will also be considered, leading to fractional moments in v and/or a reconstruction of the NDF as a function of r (see the corresponding change of variable in Appendix A).

2.3. Moment space and realizability

In order to give a clear picture of the moment space and the realizability problem, we recall some knowledge from the theory of moments. For simplicity, we drop time t hereinafter in this section.

For hybrid methods, only two moments m_0 and m_1 are considered and the space in which they live is clearly $\mathcal{M}_1(V_{\min}, V_{\max})\{(m_0, m_1) \in \mathbb{R}_+^2 \,\big|\, V_{\min} m_0 \leq m_1 \leq V_{\max} m_0\}$. If m_0 is positive, then the equalities $V_{\min} m_0 = m_1$ and $V_{\max} m_0 = m_1$ correspond to the degenerate cases where the NDF is a Dirac delta function at $V_{\min}$ or $V_{\max}$, respectively. There is no reason why such cases should appear if $V_{\min}$ and $V_{\max}$ do not coincide with the nuclei size V_{nuc}. Only the degenerate case $(m_0, m_1) = (0, 0)$ will then be considered, leading to a zero NDF.

For QBMM, the semi-infinite space $[0, \infty)$ is considered for the interval $]V_{\min}, V_{\max}[$, as well as moments of order 0 to N on this interval in the variable ξ, which is the volume v or the variable $r = v^{1/3}$. For any positive measure $\mathrm{d}\mu(\xi)$, *i.e.* induced by a nondecreasing function $\mu(\xi)$ on $[0, \infty)$, let us denote $\mathbf{m}_N(\mathrm{d}\mu)$ the vector of moments defined by

$$\mathbf{m}_N(\mathrm{d}\mu) = (m_0(\mathrm{d}\mu), m_1(\mathrm{d}\mu), \ldots, m_N(\mathrm{d}\mu))^T, \qquad m_k(\mathrm{d}\mu) = \int_0^\infty \xi^k \mathrm{d}\mu(\xi), \quad k \geq 0, \tag{7}$$

assuming that such moments are finite. One then has the following definition of the moment space:

Definition 2.1 (Moment space)**.** *The moment space $\mathcal{M}_N(0, \infty)$ is defined as the set of all moment vectors $\mathbf{m}_N(\mathrm{d}\mu)$, where $\mathrm{d}\mu(\xi)$ is a positive measure having finite moments of order 0 to N.*

To simplify the notation, $\mathcal{M}_N(0, \infty)$ is also denoted $\mathcal{M}_N$. The moment space can also be defined by the moments of the probability measure [32, 33]. Let us denote it by $\tilde{\mathcal{M}}_N$ in this case. There is a one-to-one relation between $\mathcal{M}_N - (0, \ldots, 0)^T$ and $\tilde{\mathcal{M}}_N$ through the division by the zero-order moment. Here, the zero moment vector can be used and this is why we employ the definition for positive measures.

Moment space is convex [61] and can be characterized by the Hankel determinants defined by

$$\underline{\mathcal{H}}_{2n+d} = \begin{vmatrix} m_d & \ldots & m_{n+d} \\ \vdots & \ddots & \vdots \\ m_{n+d} & \ldots & m_{2n+d} \end{vmatrix} \tag{8}$$

with $d \in \{0,1\}$ and $n \in \mathbb{N}$. Indeed, $\mathbf{m}_N = (m_0, m_1, \ldots, m_N)^T$ is in $\mathcal{M}_N$ if and only if the Hankel determinants $\underline{\mathcal{H}}_k$ are non-negative for $k \in \{0, 1, \ldots, N\}$ [32, 33]. Moreover, if one of the Hankel determinants is zero, then the moment vector is on the boundary of moment space $\partial\mathcal{M}_N$. It is then interesting to define the minimum integer k such that $\mathbf{m}_k$ is on the boundary of the kth moment space $\mathcal{M}_k$. This integer is denoted $\mathcal{N}(\mathbf{m}_N)$ and then $\underline{\mathcal{H}}_k$ is positive for $k < \mathcal{N}(\mathbf{m}_N)$, whereas $\underline{\mathcal{H}}_{\mathcal{N}(\mathbf{m}_N)} = \cdots = \underline{\mathcal{H}}_N = 0$. In this case, the only measure corresponding to this moment vector is a sum of k weighted Dirac delta functions, with $\mathcal{N}(\mathbf{m}_N) = 2k - 1$ if it is an odd number. If the considered Hankel determinants are positive, then the moment vector $\mathbf{m}_N$ is in the interior $Int(\mathcal{M}_N)$ of the moment space $\mathcal{M}_N$ and, by convention, $\mathcal{N}(\mathbf{m}_N) = N + 1$.

Since the boundary of moment space can be attained (monodisperse or discrete polydisperse cases with a small number of sizes), it is important to be able to determine $\mathcal{N}(\mathbf{m}_N)$ from a numerical point of view. In practical applications, such boundary detection with Hankel determinants is costly and can be inaccurate when the moments are close to the boundary, due to numerical errors. A more efficient algorithm can be extracted from the theory of orthogonal polynomials [32, 61, 62]. A sequence of polynomials $\{P_k\}_{i\in\mathbb{N}}$, where P_k is of exact degree k and orthogonal with respect to some positive measure $\mathrm{d}\mu(\xi)$ on the semi-infinite support $[0, \infty)$ if and only if $\int_0^\infty P_k(x)\, P_l(x)\, \mathrm{d}\mu(x) = 0$ for any $k \neq l$. It is then well known that this sequence satisfies a three-term recurrence relation of the form

$$P_{k+1}(x) = (x - a_{k+1})P_k(x) - b_{k+1}P_{k-1}(x), \qquad k \in \mathbb{N}, \tag{9}$$

with $b_{k+1} > 0$ and $P_{-1}(x) = 0$, $P_0(x) = 1$. Conversely, if the sequence of polynomials satisfies (9) with $b_{k+1} > 0$ for all $k \in \mathbb{N}$, then there exists a measure on the real line for which the polynomials are orthogonal. It is also well known [62] that the measure μ is supported on $[0, \infty)$ if and only if there exists a sequence of positive numbers $\{\zeta_n\}_{n\in\mathbb{N}^*}$ such that the coefficients in the recurrence relation (9) satisfy for all $k \geq 1$:

$$b_k = \zeta_{2k-1}\zeta_{2k}, \qquad a_k = \zeta_{2k} + \zeta_{2k+1}. \tag{10}$$

Moreover, the link between $\{\zeta_n\}_{n\in\mathbb{N}}$ and Hankel determinants [32] is given by

$$\zeta_k = \frac{\underline{\mathcal{H}}_k \underline{\mathcal{H}}_{k-3}}{\underline{\mathcal{H}}_{k-1}\underline{\mathcal{H}}_{k-2}} \tag{11}$$

where we use $\underline{\mathcal{H}}_k = 1$ if $k \leq 0$. Then, one has the following properties:

Proposition 2.2 (Realizability)**.** *Let us consider a moment vector $\mathbf{m}_N$ and the corresponding $(\zeta_k)_{k=1,\ldots,N}$. Then $\mathbf{m}_N$ is in the interior $Int(\mathcal{M}_N)$ of moment space if and only if $\zeta_k > 0$ for $k = 1, \ldots, N$. Moreover $\mathbf{m}_N$ is on the boundary $\partial\mathcal{M}_N$ of moment space, with $\mathcal{N}(\mathbf{m}_N) = n$ if and only if $\zeta_k > 0$ for $k = 1, \ldots, n-1$ and $\zeta_n = \cdots = \zeta_N = 0$.*

Several algorithms can be employed to compute efficiently the recurrence coefficients a_k and b_k and then the ζ_k from the moments: Rutishauser's QD algorithm [63, 64], Gordon's PD algorithm [65, 66] and variation of an algorithm attributed to Chebyshev and given by Wheeler in [67]. Since it is found to be slightly more stable in practice [67], the last one is used here and referred to as the Chebyshev algorithm (see Appendix B for the description of the ζ–Chebyshev algorithm, coupling this Chebyshev algorithm to the computation of the ζ_k). Moreover, one can remark that, given a moment vector $\mathbf{m}_{2n-1} \in Int(\mathcal{M}_{2n-1})$, the quadrature can be evaluated based on the tridiagonal Jacobi matrix [61] formed by the recurrence coefficients a_k and b_k. Thus, we obtain a consistent

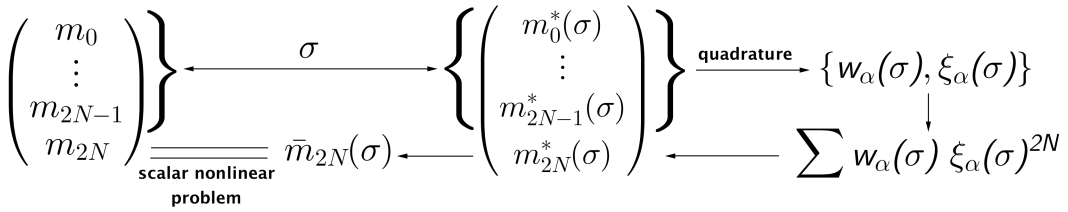

Figure 1: EQMOM moment-inversion algorithm.

and robust way to compute the quadrature and verify the realizability of an arbitrary moment set, including boundary detection.

In the rest of the paper, the less rigorous notation $f(\xi)\mathrm{d}\xi$ is used for the measure, instead of $\mathrm{d}\mu(\xi)$, making the NDF apparent.

2.4. EQMOM

When considering QBMM, the EQMOM reconstruction is able to close the moment transport equations (6), since it gives a value of the NDF at zero size. Moreover, it is able to degenerate to a sum of weighted Dirac delta functions in the case where the moment vector is on the boundary of moment space. In this section, the principle of this method is recalled, as well as two types of KDF used for the truncated Stieljes moment problem [49, 52]. Moreover, a more robust and efficient EQMOM moment-inversion algorithm is developed here, able to deal with the boundary of moment space.

2.4.1. EQMOM moment inversion

In EQMOM, the NDF is represented by weighted sum of KDF on a semi-infinite support [49]:

$$f(\xi) = \sum_{\alpha=1}^{N} w_\alpha\, \delta_\sigma(\xi, \xi_\alpha) \tag{12}$$

where σ is a unique nonnegative parameter shared by all KDF. This representation also captures the tail of the distribution corresponding to large particles. To deal with the boundary of moment space, the following informal convergence is imposed through the choice of the KDF: $\lim_{\sigma\to 0} \delta_\sigma(\xi, \xi_\alpha) = \delta(\xi - \xi_\alpha)$. Let us define $\langle\xi\rangle_{k,\alpha}$, $\mathbf{m}_n = (m_0, \ldots, m_n)^T$ and $\mathbf{m}_n^* = (m_0^*, \ldots, m_n^*)^T$, respectively, using

$$\langle\xi\rangle_{k,\alpha} = \int_0^\infty \xi^k\, \delta_\sigma(\xi, \xi_\alpha)\, \mathrm{d}v, \qquad m_k = \sum_{\alpha=1}^{N} w_\alpha \langle\xi\rangle_{k,\alpha}, \qquad m_k^* = \sum_{\alpha=1}^{N} w_\alpha \xi_\alpha^k. \tag{13}$$

A second constraint on the KDF is that for any $k \geq 1$, there exists an invertible matrix $A_k(\sigma)$, independent of the weights w_α and abscissas ξ_α such that $\mathbf{m}_k = A_k(\sigma)\mathbf{m}_k^*$. The purpose of this constraint is to allow for the use of the quadrature based on the Chebyshev algorithm. Indeed, for any value of σ, one can compute $\mathbf{m}_{2N-1}^*(\sigma) = A_{2N-1}(\sigma)^{-1}\mathbf{m}_{2N-1}$, and then use the quadrature algorithm to compute the weights $(w_\alpha(\sigma))_{\alpha=1}^N$ and abscissas $(\xi_\alpha(\sigma))_{\alpha=1}^N$ if $\mathbf{m}_{2N-1}^*(\sigma)$ is in the interior of moment space. The moments of orders 0 to $2N-1$ of the EQMOM reconstruction corresponding to these parameters for a given σ, $(w_\alpha(\sigma))_{\alpha=1}^N$ and $(\xi_\alpha(\sigma))_{\alpha=1}^N$ are m_0 to m_{2N-1},

and the value of σ has to be adapted in order that its $2N$th-order moment is m_{2N} (which is not always possible).

The original EQMOM moment-inversion algorithm is given in [49]. There are two open issues with this algorithm. First, the boundary of moment space was not really dealt with, as well as the transition with the interior of moment space since only moment vectors far from this boundary were considered. This point is however essential here for the robustness and accuracy of our computations, considering the typical solution of the PBE described in Sec. 2.1. Second, the iterative algorithm for the computation of σ was not optimal. This is why we propose an improved version of the algorithm, summarized in Fig. 1.

Here, if $\mathbf{m}_{2N}$ is in the interior of moment space, one defines the function $\bar{m}_{2N}$ of σ in the following way: if $\mathbf{m}^*_{2N-1}(\sigma) = A_{2N-1}(\sigma)^{-1}\mathbf{m}_{2N}$ is in the interior $Int(\mathcal{M}_{2N-1})$ of moment space, then one computes the corresponding quadrature weights $(w_\alpha(\sigma))_{\alpha=1}^N$ and abscissas $(\xi_\alpha(\sigma))_{\alpha=1}^N$ and one defines $m^*_{2N}(\sigma) = \sum_{\alpha=1}^{2N} w_\alpha(\sigma)\xi_\alpha(\sigma)^{2N}$. Let us denote $\mathbf{m}^*_{2N}(\sigma) = (m^*_0, \ldots, m^*_{2N})^T$. The value of $\bar{m}_{2N}(\sigma)$ is then deduced from this vector thanks to the matrix $A_{2N}(\sigma)$ (just its last line in fact):

$$\bar{m}_{2N}(\sigma) = (0, \ldots, 0, 1)A_{2N}(\sigma)\mathbf{m}^*_{2N}(\sigma).$$

If $\mathbf{m}^*_{2N-1}(\sigma)$ is not in the interior of moment space, then the value of σ is invalid. The function $\bar{m}_{2N}(\sigma)$ is then set to a very high value, *e.g.* 10^{100}, so that this case will be automatically eliminated. Hence, the value of σ is obtained by solving the following scalar nonlinear problem:

$$D_{2N}(\sigma) = 0 \quad \text{where } D_{2N}(\sigma) = m_{2N} - \bar{m}_{2N}(\sigma). \tag{14}$$

Let us remark that, in the case $N = 2$, an analytical condition on σ of the form $\sigma \leq \sigma^{(2)}_{\max}$ for the realizability of $\mathbf{m}^*_{2N-1}(\sigma)$ can usually be obtained, ensuring the non-negativity of the corresponding Hankel determinants $\underline{\mathcal{H}}^*_2$ and $\underline{\mathcal{H}}^*_3$. Moreover, $D_{2N}(0)$ is positive if $\mathbf{m}_{2N}$ is in the interior of moment space and the problem (14) either has a solution or a nonlinear solver will give the value corresponding to an upper limit $\sigma_{\max}$ for σ, when a singularity appears for the function $D_{2N}(\sigma)$. In this last case, one just has to minimize the error on the last moment by minimizing $D_{2N}(\sigma)^2$.

The global algorithm of EQMOM reconstruction from a moment vector $\mathbf{m}_{2N}$, able to deal with the boundary of moment space, is then:

1. Determine $\mathcal{N}(\mathbf{m}_{2N})$ by computing the $(\zeta_k)_{k=1,\ldots,2N}$ with the ζ-Chebyshev algorithm.
   1.1. If $\mathcal{N}(\mathbf{m}_{2N})$ is an odd number $2n-1$, then $\sigma = 0$ and the quadrature points are obtained from three-term recurrence coefficients given by the $(\zeta_k)_{k=1,\ldots,2n-1}$.
   1.2. Otherwise, let $\mathcal{N}(\mathbf{m}_{2N}) = 2n$ where $n \leq N$ and move to step 2.
2. Solve the scalar nonlinear problem (14) in the interval $]0, \sigma^{(2)}_{\max}[$ using Ridders' method [68].
   2.1. If $D_{2n}(\sigma) = 0$ then go to step 4.
   2.2. Otherwise, in case of not being able to obtain σ, set $\sigma_{\max} = \sigma$ and go to step 3.
3. Use Brent's method [68] on $[0, \sigma_{max}]$ to minimize $D_{2n}(\sigma)^2$.
4. Once the parameter σ is obtained, the weights and abscissas are computed with the quadrature algorithm, from $\mathbf{m}^*_{2n-1} = A_{2n-1}(\sigma)^{-1}\mathbf{m}_{2n-1}$.

Two types of KDF are considered for the Stieljes problem: gamma [49] and log-normal [52]. The matrix $A_k(\sigma)$ can then be given explicitly, as well as the interval on which σ is located.

2.4.2. Gamma-EQMOM

The gamma KDF reads

$$\delta_\sigma(\xi,\xi_\alpha) = \frac{\xi^{k_\alpha-1}\, e^{-\xi/\sigma}}{\Gamma(k_\alpha)\,\sigma^{k_\alpha}} \tag{15}$$

where $\Gamma(\cdot)$ is the gamma function, $\sigma > 0$, $k_\alpha > 0$ and $k_\alpha = \xi_\alpha/\sigma$. The moment of order k of the gamma KDF is given by

$$\langle\xi\rangle_{k,\alpha} = \begin{cases} 1, & \text{if } k = 0, \\ \displaystyle\sum_{i=1}^{k} a_{ki}\,\xi_\alpha^i\,\sigma^{k-i}, & \text{if } k \geq 1, \end{cases} \tag{16}$$

where $a_{k,k} = 1$ and a_{ki} is given by the following recurrence formula:

$$a_{ki} = (k-1)a_{k-1i} + a_{k-1i-1} \qquad k = 1,\ldots,2N-1; \quad i = 2,\ldots,k-1. \tag{17}$$

Thus, $A_k(\sigma)$ is a triangular matrix of coefficients $[A_k(\sigma)]_{i,j} = a_{ij}\sigma^{i-j}$ for $0 \leq j \leq i$, which can be easily inverted. Moreover, the coefficients a_{ij} can be precomputed and stored.

Finally, the maximum value for σ, in the case $N = 2$ is given by

$$\sigma_{\max}^{(2)} = \min\left\{\frac{m_2m_0 - m_1^2}{m_0m_1}, \frac{m_3m_1 - m_2^2}{m_1m_2}\right\}. \tag{18}$$

2.4.3. Ln-EQMOM

The log-normal (Ln) KDF reads

$$\delta_\sigma(\xi,\xi_\alpha) = \frac{\exp[-(\ln\xi - \ln\xi_\alpha)^2/2\sigma^2]}{\xi\,\sigma\sqrt{2\pi}} \tag{19}$$

where σ and ξ_α are positive. The moment of order k of the Ln KDF is $\langle\xi\rangle_{k,\alpha} = \xi_\alpha^k e^{k^2\sigma^2/2}$. The matrix $A_k(\sigma)$ is a diagonal matrix of coefficients $[A_k(\sigma)]_{i,i} = e^{i^2\sigma^2/2}$ so that the relation between $\mathbf{m}_k$ and $\mathbf{m}_k^*$ is easy to compute.

Moreover, a change of variable is used in (14). The nonlinear problem is then solved for $b = e^{\sigma^2/2}$, in the interval $]1, b_{\max}^{(2)}[$, with

$$b_{\max}^{(2)} = \min\left\{\frac{\sqrt{m_0m_2}}{m_1}, \frac{\sqrt{m_1m_3}}{m_2}\right\}. \tag{20}$$

2.5. TSM method

For TSM, a discretization $0 = V_0 < V_1 < \ldots < V_{N_s} = +\infty$ is introduced. On each section $I_k = [V_{k-1}, V_k]$, the moments of orders 0 and 1 in volume are considered:

$$N_k = \int_{V_{k-1}}^{V_k} f(v)\,\mathrm{d}v, \qquad M_k = \int_{V_{k-1}}^{V_k} v\,f(v)\,\mathrm{d}v. \tag{21}$$

Physically, they are usually the main variables of interest since the global moment of order 0 is conserved by the growth term and the global moment of order 1 is conserved by aggregation, for example. This is one of the advantages of the hybrid TSM method over standard sectional

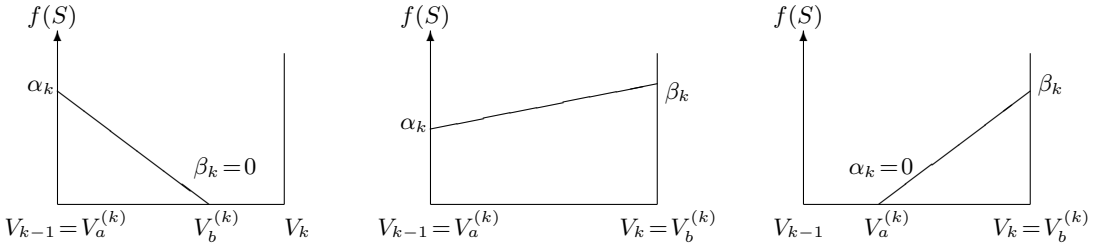

Figure 2: The three possible TSM reconstructions.

$\frac{M_k}{N_k} \in$	$\left]V_k, V_{\min}^{(k)}\right[$	$\left[V_{\min}^{(k)}, V_{\max}^{(k)}\right]$	$\left[V_{\max}^{(k)}, V_k\right[$
$V_a^{(k)}$	V_{k-1}	V_{k-1}	$3\frac{M_k}{N_k} - 2V_k$
$V_b^{(k)}$	$3\frac{M_k}{N_k} - 2V_{k-1}$	V_k	V_k
α_k	$\frac{2N_k}{V_b^{(k)} - V_{k-1}}$	$\frac{6}{(V_k - V_{k-1})^2}\left(V_{\max}^{(k)} N_k - M_k\right)$	0
β_k	0	$\frac{6}{(V_k - V_{k-1})^2}\left(-V_{\min}^{(k)} N_k + M_k\right)$	$\frac{2N_k}{V_k - V_a^{(k)}}$

Table 1: Coefficients of the TSM reconstruction in v, depending of the ratio M_k/N_k.

methods, where a single variable has to be chosen, thus usually loosing some conservation properties. Moreover, the last section here is semi-infinite: the size domain does not have to be bounded, as it must be for the standard sectional methods.

In practice, the change of variable $v = r^3$ can be interesting to consider when dealing with size reduction. Indeed, the variable $r = v^{1/3}$ then decreases at a constant rate, making it the best variable for describing such phenomena [28, 34]. The considered variables are then moments of orders 0 and 3 of the corresponding NDF: $f^r(r)$ (with $f^r(r)\mathrm{d}r = f(v)\mathrm{d}v$):

$$N_k = \int_{R_{k-1}}^{R_k} f^r(r)\,\mathrm{d}r, \qquad M_k = \int_{R_{k-1}}^{R_k} r^3\, f^r(r)\,\mathrm{d}r, \tag{22}$$

with $R_k^3 = V_k$ for $k \geq 0$. So the two types of reconstruction, using variable v or r, are considered in this work.

2.5.1. v-reconstruction

The NDF is approximated by an affine function on each section I_k:

$$f(v)|_{I_k} = \left[\alpha_k + (\beta_k - \alpha_k)\frac{v - V_a^{(k)}}{V_b^{(k)} - V_a^{(k)}}\right] \mathbb{1}_{[V_a^{(k)}, V_b^{(k)}]}(v). \tag{23}$$

We consider three cases represented in Fig. 2:

1. $V_a^{(k)} = V_{k-1}$, $V_b^{(k)} < V_k$ and $\beta_k = 0$.

$\frac{M_k}{N_k} \in$	$\left]V_k, V_{\min}^{(k)}\right[$	$\left[V_{\min}^{(k)}, V_{\max}^{(k)}\right]$	$\left[V_{\max}^{(k)}, V_k\right[$
$R_a^{(k)}$	R_{k-1}	R_{k-1}	$R_k^{(1)}$
$R_b^{(k)}$	$R_k^{(2)}$	R_k	R_k
α_k	$\dfrac{2N_k}{R_b^{(k)} - R_{k-1}}$	$\dfrac{2}{(R_k - R_{k-1})\left(V_{\max}^{(k)} - V_{\min}^{(k)}\right)}\left(V_{\max}^{(k)} N_k - M_k\right)$	0
β_k	0	$\dfrac{2}{(R_k - R_{k-1})\left(V_{\max}^{(k)} - V_{\min}^{(k)}\right)}\left(-V_{\min}^{(k)} N_k + M_k\right)$	$\dfrac{2N_k}{R_k - R_a^{(k)}}$

Table 2: Coefficients of the TSM reconstruction in r, depending of the ratio M_k/N_k.

2. $V_a^{(k)} = V_{k-1}$ and $V_b^{(k)} = V_k$.
3. $V_a^{(k)} > V_{k-1}$, $V_b^{(k)} = V_k$ and $\alpha_k = 0$.

The coefficients α_k, β_k, $V_a^{(k)}$ and $V_b^{(k)}$ have to be determined in such a way that the moments of orders 0 and 1 on I_k of f are N_k and M_k, respectively. Let us define the two following mean volumes:

$$V_{\min}^{(k)} = \frac{V_k + 2V_{k-1}}{3}, \qquad V_{\max}^{(k)} = \frac{2V_k + V_{k-1}}{3}.$$

For any N_k and M_k such that $0 < V_{k-1}N_k < M_k < V_k N_k$, the value of the coefficients are given in Table 1, depending of the ratio M_k/N_k [29].

2.5.2. r-reconstruction

When considering the r variable, the NDF is approximated by the following function on each section I_k:

$$f^r(r)|_{I_k} = \left[\alpha_k + (\beta_k - \alpha_k)\frac{r - R_a^{(k)}}{R_b^{(k)} - R_a^{(k)}}\right] \mathbb{1}_{[R_a^{(k)}, R_b^{(k)}]}(r) \tag{24}$$

with three possible cases:

1. $R_a^{(k)} = R_{k-1}$, $R_b^{(k)} < R_k$ and $\beta_k = 0$.
2. $R_a^{(k)} = R_{k-1}$ and $R_b^{(k)} = R_k$.
3. $R_a^{(k)} > R_{k-1}$, $R_b^{(k)} = R_k$ and $\alpha_k = 0$.

The coefficients α_k, β_k, $R_a^{(k)}$ and $R_b^{(k)}$ have to be determined in such a way that the moments of orders 0 and 3 on I_k of f^r are N_k and M_k, respectively. Let us define the following two mean volumes:

$$V_{\min}^{(k)} = 2\int_{R_{k-1}}^{R_k} r^3 \frac{R_k - r}{(R_k - R_{k-1})^2}\mathrm{d}r = \frac{4R_{k-1}^3 + 3R_{k-1}^2 R_k + 2R_{k-1}R_k^2 + R_k^3}{10} \tag{25a}$$

$$V_{\max}^{(k)} = 2\int_{R_{k-1}}^{R_k} r^3 \frac{r - R_{k-1}}{(R_k - R_{k-1})^2}\mathrm{d}r = \frac{4R_k^3 + 3R_k^2 R_{k-1} + 2R_k R_{k-1}^2 + R_{k-1}^3}{10} \tag{25b}$$

For any N_k and M_k such that $0 < V_{k-1}N_k < M_k < V_kN_k$, the value of the coefficients are given in Table 2, depending of the ratio M_k/N_k, with

$$R_k^{(1)} = \left[\frac{5}{27}\left(-7R_k^3 + 27\frac{M_k}{N_k} + \sqrt{\left(-7R_k^3 + 27\frac{M_k}{N_k}\right)^2 + 5R_k^6}\right)\right]^{1/3} + \left[\frac{5}{27}\left(-7R_k^3 + 27\frac{M_k}{N_k} - \sqrt{\left(-7R_k^3 + 27\frac{M_k}{N_k}\right)^2 + 5R_k^6}\right)\right]^{1/3} - \frac{2R_k}{3} \quad (26a)$$

$$R_k^{(2)} = \left[\frac{5}{27}\left(-7R_{k-1}^3 + 27\frac{M_k}{N_k} + \sqrt{\left(-7R_{k-1}^3 + 27\frac{M_k}{N_k}\right)^2 + 5R_{k-1}^6}\right)\right]^{1/3} + \left[\frac{5}{27}\left(-7R_{k-1}^3 + 27\frac{M_k}{N_k} - \sqrt{\left(-7R_{k-1}^3 + 27\frac{M_k}{N_k}\right)^2 + 5R_{k-1}^6}\right)\right]^{1/3} - \frac{2R_{k-1}}{3} \quad (26b)$$

3. Continuous particle-size changes

We now demonstrate accurate and realizable schemes for the description of continuous particle-size changes. They are based on the scheme developed for spray evaporation with moment methods by Massot et al. [34], and adapted to TSM by Laurent et al. [29]. However, for moment methods, this scheme was developed for an even number of moments. An adaptation is done here, based on the interpretation given in [29] of the scheme as an evaluation by a quadrature method of the integrals deduced from a kinetic scheme. Therefore, the kinetic scheme and the analytical solution of the PBE on which it is based are first recalled. Then, the quadrature-kinetic scheme (QKS) is given for both EQMOM and TSM. The ability of the two methods to describe continuous particle-size changes is then evaluated, separately for size reduction and growth.

3.1. Analytical solution and kinetic scheme

The rate is denoted by $\mathcal{R}$ in general for both growth and size reduction. The PBE then reads

$$\partial_t f(t,\xi) + \partial_\xi \left[\mathcal{R}(t,\xi) f(t,\xi)\right] = 0 \quad (27)$$

where ξ can be volume v or the variable $r = v^{1/3}$. If $f(0,\xi) = f_0(\xi)$ is the initial NDF, then the analytical solution of this equation is given by

$$f(t,\xi) = f_0(\Xi(0;t,\xi))J(0;t,\xi) \quad (28)$$

where the characteristics $\Xi(t;s,\xi)$ of (27) are defined by the evolution of particle size:

$$\frac{d\Xi(t;s,\xi)}{dt} = \mathcal{R}(\Xi) \quad \text{with} \quad \Xi(s;s,\xi) = \xi, \quad (29)$$

and $J(t;s,\xi)$ is the Jacobian of the transformation $\xi \mapsto \Xi(t;s,\xi)$.

In case of continuous reduction of particle size (3), if the coefficient c_{red} is constant, then the analytical solution is given, using the volume for ξ, by

$$f(t,v) = f_0\left(\left[v^{1/3} + \frac{c_{\mathrm{red}}}{3}t\right]^3\right)\frac{\left(v^{1/3} + \frac{c_{\mathrm{red}}}{3}t\right)^2}{v^{2/3}}, \tag{30}$$

since the characteristics are given by

$$\Xi(t;s,v) = \left[v^{1/3} - \frac{c_{\mathrm{red}}}{3}(t-s)\right]^3. \tag{31}$$

Let us remark that, when considering r instead of v and starting from a r-NDF f_0^r, the solution is

$$f^r(t,r) = f_0^r\left(r + \frac{c_{\mathrm{red}}}{3}t\right) \tag{32}$$

For diffusion-controlled growth (4), we obtain, when the coefficient c_{gro} is constant, the following analytical solution, using the volume for ξ:

$$f(t,v) = f_0\left(\left[v^{2/3} - \frac{2}{3}c_{\mathrm{gro}}t\right]^{3/2}\right)\frac{\sqrt{v^{2/3} - \frac{2}{3}c_{\mathrm{gro}}t}}{v^{1/3}}, \tag{33}$$

since the characteristics are given by

$$\Xi(t;s,v) = \left[v^{2/3} + \frac{2}{3}c_{\mathrm{gro}}(t-s)\right]^{3/2}. \tag{34}$$

Using the variable $r = v^{1/3}$ for ξ, we find

$$f^r(t,r) = f_0^r\left(\sqrt{r^2 - \frac{2}{3}c_{\mathrm{gro}}t}\right)\frac{r}{\sqrt{r^2 - \frac{2}{3}c_{\mathrm{gro}}t}}. \tag{35}$$

The principle of the kinetic scheme is to use the exact solution of the PBE inside a time step. Then, from the moments at time t_n, a NDF $f_n(\xi)$ is reconstructed for $\xi \in \mathbb{R}_+$, using the algorithms given in Sec. 2.4 for EQMOM and in Sec. 2.5 for TSM. The exact solution of the PBE (27) between t_n and t_{n+1} starting from this NDF is $f(t,\xi) = f_n(\Xi(t_n;t,\xi))J(t_n;t,\xi)$. The moments at time t_{n+1} are deduced from the NDF $f(t_{n+1},\xi)$. Since they are moments on some interval $]\xi_{\min},\xi_{\max}[$ of the NDF, they are written as

$$\int_{\xi_{\min}}^{\xi_{\max}} \xi^k f_n(\Xi(t_n;t_{n+1},\xi))J(t_n;t_{n+1},\xi)\mathrm{d}\xi = \int_{\Xi(t_n;t_{n+1},\xi_{\min})}^{\Xi(t_n;t_{n+1},\xi_{\max})} (\Xi(t_{n+1};t_n,\zeta))^k f_n(\zeta)\mathrm{d}\zeta \tag{36}$$

where the second expression is obtained thanks to the change of variable $\zeta = \Xi(t_n;t_{n+1},\xi)$, equivalent to $\xi = \Xi(t_{n+1};t_n,\zeta)$. Depending of the complexity of $\mathcal{R}(t,\xi)$, the solution and its moments are not always easy to compute analytically. This is why the QKS scheme is used.

3.2. QKS

The principle of QKS is the same as the kinetic scheme, except that the integrals (36) are now evaluated thanks to a Gauss quadrature of the measure $f_n(\zeta)\mathbb{1}_{]\Xi(t_n;t_{n+1},\xi_{\min}),\Xi(t_n;t_{n+1},\xi_{\max})[}(\zeta)\mathrm{d}\zeta$. Indeed, from the moments of orders 0 to $2N+1$ of f_n on the interval $]\Xi(t_n;t_{n+1},\xi_{\min}),\Xi(t_n;t_{n+1},\xi_{\max})[$, quadrature points $\{w_\alpha,\xi_\alpha\}_{\alpha=1,}^{N+1}$ are determined and the previous integral is approximated by

$$\sum_{\alpha=1}^{N+1} w_\alpha\ \Xi(t_{n+1};t_n,\xi_\alpha)^k. \tag{37}$$

The number N is equal to 1 for TSM, and corresponds to the number of KDF used for EQ-MOM. Using at least $N+1$ quadrature points is essential so that the moment vector at time t_{n+1} is in the interior of the corresponding moment space. Moreover, if the abscissas ξ_α belong to $]\Xi(t_n;t_{n+1},\xi_{\min}),\Xi(t_n;t_{n+1},\xi_{\max})[$, then $\Xi(t_{n+1};t_n,\xi_\alpha)$ belongs to $]\xi_{\min},\xi_{\max}[$ and the scheme is realizable. Then, the ODE (29) defining the characteristics has to be solved once in reverse time to compute each bound $\Xi(t_n;t_{n+1},\xi_{\min})$, when the result is nontrivial, and $N+1$ times to determine the evolution of the quadrature abscissas. In a one-way coupling context, this can be done easily, even if the drift rate is time dependent due to a dependence on the gas variables. In a two-way coupling context with a time-dependent drift rate, either the evolution of the drift term during the time step can be estimated or it is set constant.

3.2.1. QBMM

For QBMM, the evolution of the moments due to continuous size reduction is as follows:

1. Given the moment set $\left\{m_k^n\right\}_{k=0}^{2N}$ at time t_n, reconstruct a NDF $f_n(\xi)$.
2. Compute the moments $\left\{\tilde{m}_k\right\}_{k=0}^{2N+1}$ of f_n on $]\Xi(t_n;t_{n+1},0),\infty[$: $\tilde{m}_k=\int_{\Xi(t_n;t_{n+1},0)}^{\infty}\xi^k f_n(\xi)\mathrm{d}\xi$.
3. Compute quadrature points to obtain $\{w_\alpha,\xi_\alpha\}_{\alpha=1}^{N+1}$ from the new moment set $\left\{\tilde{m}_k\right\}_{k=0}^{2N+1}$.
4. Update the moment set thanks to the characteristics

$$m_k^{n+1}=\sum_{\alpha=1}^{N+1} w_\alpha\ \Xi(t_{n+1};t_n,\xi_\alpha)^k,\qquad k=0,\dots,2N. \tag{38}$$

Let us remark that the moments $\tilde{m}_k$ are computed analytically. The moments of the NDF between 0 and $\Xi(t_n;t_{n+1},0)$ correspond to the disappearance fluxes. When considering surface growth, these fluxes are zero and $\tilde{m}_k=m_k$. The same algorithm can be used, then computing one more moment m_{2N+1} and the N corresponding quadrature points. However, instead of these quadrature points, the secondary quadrature defined in Sec. 4 can be used, as soon as the number of secondary quadrature points N_α is greater than $N+1$. This was done in [49], which required solving the ODE $N\times N_\alpha$ times. The use of secondary quadrature points with a suitability chosen N_α is especially recommended for cases where the function $\mathcal{R}(t,\xi)$ takes on both positive (growth) and negative (size reduction) values for varying ξ, as soon as there is no disappearance fluxes.

3.2.2. TSM

For TSM, the scheme is similar, but dividing the interval $]\Xi(t_n;t_{n+1},\xi_{\min}),\Xi(t_n;t_{n+1},\xi_{\max})[$ into two sub-intervals on which the reconstructed NDF is smooth. This allows for a better accuracy of the scheme [29]. Let us denote by $V(\xi)$ the volume corresponding to the variable ξ (*i.e.* $V(v)=v$ and $V(r)=r^3$) and Ξ_k the bounds of the sections in terms of the variable ξ, in such a way that $V(\Xi_k)=V_k$. Then, the evolution of the moments through continuous size reduction is as follows:

1. Given the moments $\{N_k^n, M_k^n\}_{k=1}^{N_s}$ at time t_n, reconstruct a NDF $f_n(\xi)$.
2. Compute the moments of orders 0 to 3 of f_n on each interval $[\Xi(t_n; t_{n+1}, \Xi_{k-1}), \Xi_k]$ and on $[\Xi_k, \Xi(t_n; t_{n+1}, \Xi_k)]$ and the corresponding quadrature points $\{w_\alpha^{(k,I)}, \xi_\alpha^{(k,I)}\}_{\alpha=1}^2$ and $\{w_\alpha^{(k,II)}, \xi_\alpha^{(k,II)}\}_{\alpha=1}^2$.
3. Update the moments on section k: $N_k^{n+1} = \sum_{\alpha=1}^2 w_\alpha^{(k,I)} + \sum_{\alpha=1}^2 w_\alpha^{(k,II)}$ and

$$M_k^{n+1} = \sum_{\alpha=1}^{2} w_\alpha^{(k,I)} V\big[\Xi(t_{n+1}; t_n, \xi_\alpha^{(k,I)})\big] + \sum_{\alpha=1}^{2} w_\alpha^{(k,II)} V\big[\Xi(t_{n+1}; t_n, \xi_\alpha^{(k,II)})\big].$$

A similar scheme is employed for growth, but using the two intervals $[\Xi(t_n; t_{n+1}, \Xi_{k-1}), \Xi_{k-1}]$ and $[\Xi_{k-1}, \Xi(t_n; t_{n+1}, \Xi_k)]$ in step 2.

Let us remark that the time step $\Delta t_n = t_{n+1} - t_n$ has to be limited in order for the obtained moment set to stay in moment space. Indeed, the value $\Xi(t_{n+1}; t_n, \xi)$ has to stay in $[\Xi_{k-1}, \Xi_k]$ if the variable ξ is in $[\Xi(t_n; t_{n+1}, \Xi_{k-1}), \Xi(t_n; t_{n+1}, \Xi_k)]$. In the case of a size-reduction rate given by (3) or for the growth rate given by (4), this is realized, respectively, through the following conditions:

$$\max_{k\in\{1,\dots,N_s\}} \frac{c_{\mathrm{red}}\Delta t_n}{3(V_k^{1/3} - V_{k-1}^{1/3})} \le 1 \qquad \max_{k\in\{1,\dots,N_s\}} \frac{2c_{\mathrm{gro}}\Delta t_n}{3(V_k^{2/3} - V_{k-1}^{2/3})} \le 1. \tag{39}$$

The coefficient on the left-hand side of each inequality is called here the CFL number.

3.3. Numerical results for size reduction

We discuss in this section numerical results for continuous size reduction using EQMOM and TSM. The initial NDF is the sum of two log-normal distributions:

$$f_0(v) = w_1 \frac{\exp[-(\ln v - \mu_1)^2/2\sigma_1^2]}{v\,\sigma_1\sqrt{2\pi}} + w_2 \frac{\exp[-(\ln v - \mu_2)^2/2\sigma_2^2]}{v\,\sigma_2\sqrt{2\pi}} \tag{40}$$

where $w_1 = w_2 = 0.5$, $\mu_1 = 3$, $\mu_2 = 0$, $\sigma_1 = 0.1$ and $\sigma_2 = 1$. The initial NDF is bimodal, as is typical of the ones induced by nucleation and aggregation. The size-reduction rate is given by (3) with $c_{\mathrm{red}} = 50$. The analytical solution is given by (30). The simulations are done for time t between 0 and $T = 0.1$.

The results of the simulations are compared to the analytical solution. Some global quantities are considered: the global v-moments m_0, m_1, m_2, the average volume m_1/m_0, and the variance $\sigma_v^2 = \frac{m_2 m_0 - m_1^2}{m_0^2}$. The maximum values in time of the errors between numerical q_{nu} and exact q_{ex} quantities, normalized by the maximal value of the exact solution are computed:

$$\mathrm{err}_q = \frac{\max_{t\in[0,T]} |q_{\mathrm{nu}}(t) - q_{\mathrm{ex}}(t)|}{\max_{t\in[0,T]} q_{\mathrm{ex}}(t)}. \tag{41}$$

Moreover, the reconstructed NDF, $f_{\mathrm{nu}}(t, v)$, as well as the corresponding volume density function (VDF) $v f_{\mathrm{nu}}(t, v)$ are also compared with the exact solution, $f_{\mathrm{ex}}(t, v)$ and $v f_{\mathrm{ex}}(t, v)$, respectively. The maximal value of the L_1 norm of the difference between the computed and exact functions, normalized by the maximal value of the L_1 norm of the exact solution, is then computed:

$$\mathrm{err}_{NDF} = \frac{\max_{t\in[0,T]} \int_0^\infty |f_{\mathrm{nu}}(t, v) - f_{\mathrm{ex}}(t, v)|\,\mathrm{d}v}{\max_{t\in[0,T]} \int_0^\infty f_{\mathrm{ex}}(t, v)\,\mathrm{d}v} \tag{42}$$

$$\mathrm{err}_{VDF} = \frac{\max_{t\in[0,T]} \int_0^\infty v\,|f_{\mathrm{nu}}(t, v) - f_{\mathrm{ex}}(t, v)|\,\mathrm{d}v}{\max_{t\in[0,T]} \int_0^\infty v f_{\mathrm{ex}}(t, v)\,\mathrm{d}v} \tag{43}$$

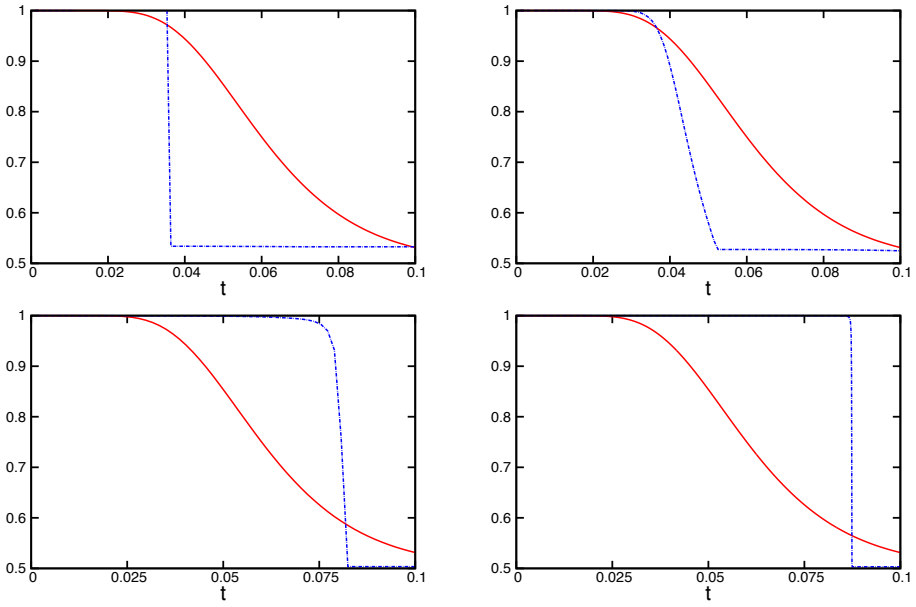

Figure 3: Evolution of m_0 for size reduction using v-reconstruction: exact (solid red line) and numerical (dashed blue line) solutions. Ln-EQMOM $N = 4$ (top left). Gamma-EQMOM $N = 4$ (top right). TSM with 41 sections: CFL=0.9 (bottom left) and CFL=0.05 (bottom right).

3.3.1. Use of v-reconstruction

Computations are done with gamma- and Ln-EQMOM with a reconstruction in v using $N = 4$ KDF. The considered moments in v are $(m_k)_{k=0}^{8}$. TSM is also used with a uniform discretization in the volume between $V_0 = 0$ and $V_{N_s-1} = V_{\max}$, the last section being $]V_{\max}, \infty[$. The number of sections is $N_s = 41$ and $V_{\max} = 50$. QKS is used with a constant time step given by $\Delta t = 0.001$, corresponding to a CFL of 0.05 for TSM. A second time step $\Delta t = 0.018$ is also used for TSM, corresponding to a larger CFL, equal to 0.9.

In all the cases, the global moments of orders 1, 2 and 3 (not shown) are well reproduced by all methods. However, the errors on the 0^{th}-order moment, plotted in Fig. 3 can attain 30 to 45 %, depending on the simulation. Moreover, this error does not decrease with the time step (it actually increases for TSM). When looking at the NDF reconstruction (see Fig. 4 corresponding to $t = 0.033$), one can see that the shape of this function is well captured by TSM, except an accumulation at zero size in the first section, whereas a shift is observed for EQMOM. This is due to the singularity in the exact solution (30) at $v = 0$. Indeed, the reconstructed NDF is regular at $v = 0$ for TSM, equal to zero at $v = 0$ for Ln-EQMOM and either equal to zero or singular at $v = 0$ for gamma-EQMOM. In all cases, the behavior at $v = 0$ is very different compared to the exact solution, which behaves like $v^{-2/3}$. This means that even if the considered moments had good values, the reconstruction close to zero would be far from the real one and the evolution of m_0 would then be badly reproduced. This also explains the accumulation of particles of small size until some time-step dependent time when they suddenly disappear. For gamma-EQMOM, the effect is smoother due to the possible singularity at zero. For TSM, it concerns only the first section, which is why the NDF is well reproduced in this case, except close to zero, even with a wrong value for

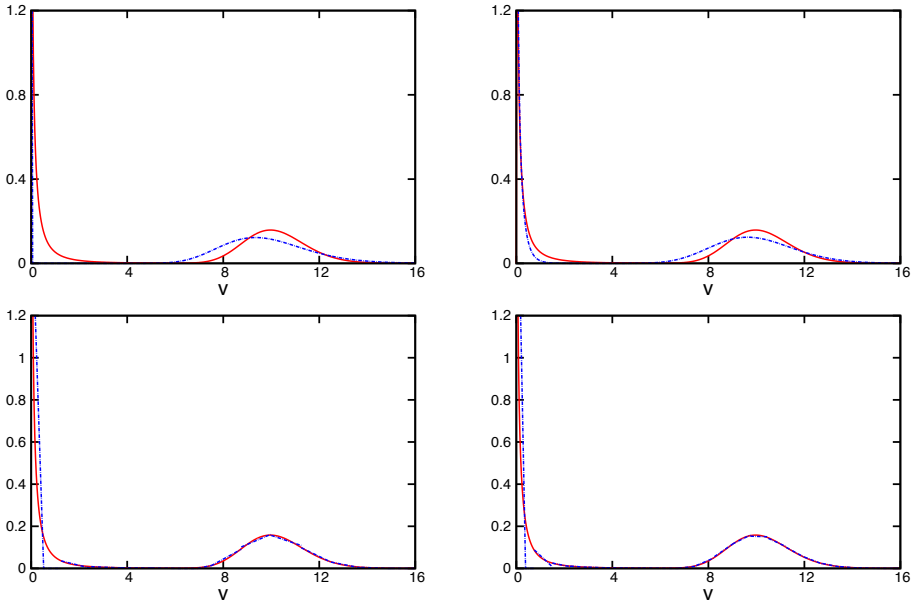

Figure 4: NDF at $t = 0.033$ for size reduction using v-reconstruction: exact (solid red line) and numerical (dashed blue line) solutions. Ln-EQMOM $N = 4$ (top left). Gamma-EQMOM $N = 4$ (top right). TSM with 41 sections: CFL=0.9 (bottom left) and CFL=0.05 (bottom right).

the global 0^{th}-order moment. In order to overcome this issue, we use the $r = v^{1/3}$ variable so that the exact NDF turns out to be advection of the initial NDF in phase space.

3.3.2. Numerical results with r-reconstruction

The computations are repeated with gamma- and Ln-EQMOM using the variable r and $N = 2$, 3 and 4 KDFs. The considered moments in v are $(m_{k/3})_{k=0}^{2N}$ and f^r is now reconstructed. TSM is also used with the same moments as in the previous section, but with a reconstruction in r and several uniform discretizations in r between $R_0 = 0$ and $R_{N_s-1} = R_{\max}$, the last section being $[R_{\max}, \infty[$, where $R_{\max} = V_{\max}^{1/3}$ and $V_{\max} = 50$. A sectional method, called the one-size moment (OSM) method, is also used, considering the same kind of discretization as TSM (without the last section, which is almost empty), using the variables M_k and a constant reconstruction in the variable r. For all methods, QKS is employed with a constant time step, $\Delta t = 0.001$, small enough so that the simulations are converged in time.

The errors induced by the EQMOM simulations are gathered on Table 3, showing first that these methods reproduce accurately the moments of orders 1 and 2 in v. The error on the 0^{th}-order moment is smaller than with the v-reconstruction, but it is still between 14 and 23 % for Ln-EQMOM, and 10 and 16 % for gamma-EQMOM. When looking at the evolution of m_0 for $N = 4$ (see Fig. 5), one observes a discontinuous behavior for Ln-EQMOM, with four discontinuities, corresponding to some discontinuities of the abscissas (see Fig. 6-left). Indeed, in this case, the reconstructed NDF is always equal to zero at zero size. The corresponding fluxes are then very small, especially if the time step is small. But size reduction induces in particular a decrease of the first abscissa and then a concentration of the first KDF close to zero, making it suddenly disappear

	Ln-EQMOM			gamma-EQMOM		
N	2	3	4	2	3	4
m_0	0.23	0.15	0.14	0.16	0.11	0.10
m_1	1.2×10^{-3}	1.5×10^{-4}	10^{-4}	1.2×10^{-3}	1.5×10^{-4}	9.3×10^{-5}
m_2	-	1.9×10^{-5}	5.8×10^{-6}	-	1.8×10^{-5}	5.5×10^{-6}
$\frac{m_1}{m_0}$	0.13	6.8×10^{-2}	7.5×10^{-2}	8.6×10^{-2}	5.8×10^{-2}	5.1×10^{-2}
σ_v^2	-	1.3×10^{-2}	1.6×10^{-2}	-	1.1×10^{-2}	9.6×10^{-3}
NDF	1.6	1.1	1.0	1.2	0.82	0.69
VDF	0.97	0.33	0.28	0.95	0.31	0.27

Table 3: Normalized L^∞ norm in time of errors for size reduction with EQMOM using r-reconstruction.

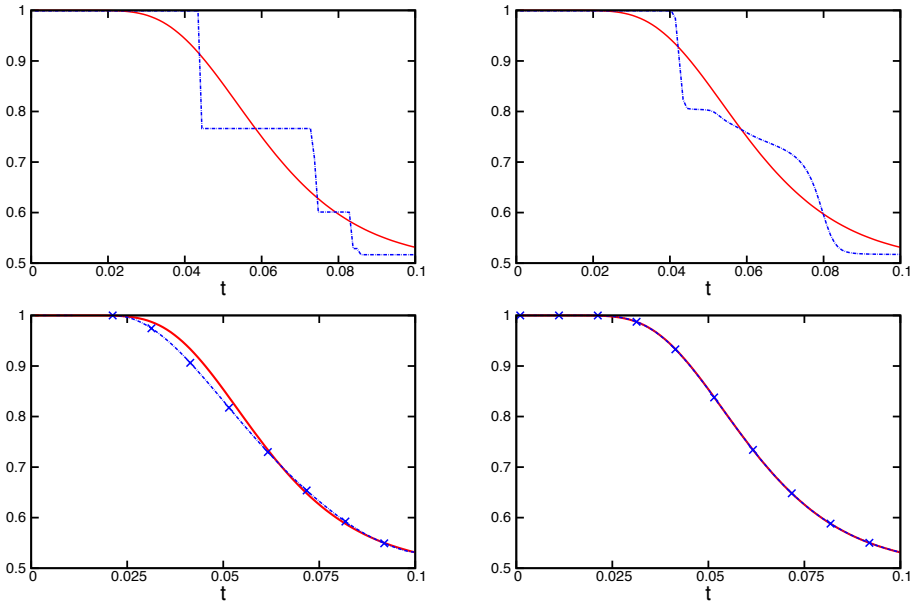

Figure 5: Evolution of m_0 for size reduction using r-reconstruction: exact (solid red line) and numerical (dashed blue line) solutions. Ln-EQMOM $N = 4$ (top left). Gamma-EQMOM $N = 4$ (top right). TSM with 9 (bottom left) and 41 sections (bottom right).

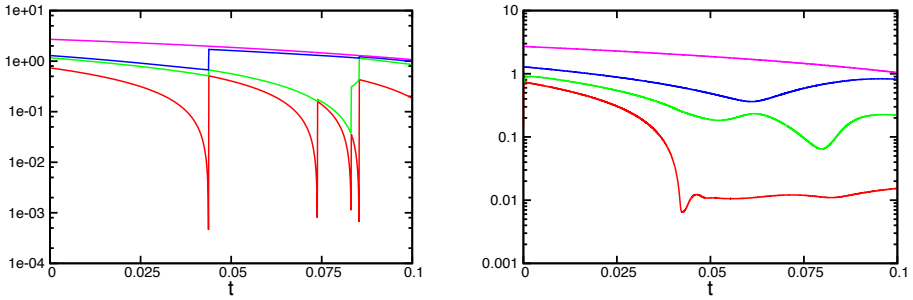

Figure 6: Size reduction using r-reconstruction. Abscissas of Ln-EQMOM (left) and gamma-EQMOM (right) with $N = 4$. Red: v_1. Green: v_2. Blue: v_3. Magenta: v_4.

	OSM			TSM			
N_s	10	18	82	5	9	21	41
m_0	0.12	0.11	2.7×10^{-2}	8.2×10^{-2}	2.8×10^{-2}	3.8×10^{-3}	5.5×10^{-4}
m_1	2.4×10^{-2}	1.5×10^{-5}	2.2×10^{-3}	7.5×10^{-3}	2.8×10^{-3}	4.6×10^{-4}	4.4×10^{-5}
m_2	0.40	0.38	0.34	4.4×10^{-2}	1.4×10^{-2}	1.5×10^{-3}	8.1×10^{-5}
$\frac{m_1}{m_0}$	7.8×10^{-2}	6.5×10^{-2}	1.3×10^{-2}	4.4×10^{-2}	1.4×10^{-2}	1.9×10^{-3}	2.5×10^{-4}
σ_v^2	1.7	1.3	1.3	0.10	3.1×10^{-2}	3.5×10^{-3}	2.2×10^{-4}
NDF	1.3	1.4	0.85	1.4	1.0	0.42	0.18
VDF	2.0	1.7	0.89	1.5	1.1	0.44	0.19

Table 4: Normalized L^∞ norm in time of errors for size reduction with TSM using r-reconstruction.

when it is too small (and the moment set is then briefly close to the boundary of the moment space, also showing the robustness of the reconstruction algorithm). With gamma-EQMOM, the evolution of m_0 as well as the abscissas is smoother (see Fig. 6-right) thanks to the possibility of the reconstruction to not be zero, even if it is singular in this case (but the flux itself is not singular thanks to the integration over a small interval).

Concerning TSM, errors for three discretizations ($N_s = 5, 9, 41$) are given in Table 4. When compared to gamma-EQMOM with $N = 4$ (using 9 moments), which gives the best results among the EQMOM simulations, TSM with only 5 sections (10 variables) is less accurate for m_1 and m_2, but gives slightly better accuracy on m_0 and on the mean volume m_1/m_0, with errors close to 8 % and 4 % respectively. The accuracy, however, rapidly increases with the number of sections, as shown in Fig. 7, where the errors on m_0, m_1 and m_2 are plotted as functions of the section size, using 3 to 65 sections. One then sees at least second-order accuracy for TSM. TSM is compared to OSM. In Table 4, errors induced by OSM for $N_s = 10, 18, 82$ are shown, thus using double the number of sections and then the same number of variables as TSM. The errors on all quantities are higher than with TSM and the convergence, when increasing the number of sections, is slow (first-order accuracy for m_1 and m_0 and smaller order for m_2, as shown on Fig. 7).

The NDF $f(t, v)$ at $t = 0.033$ is plotted on Fig. 8, from the reconstruction $f^r(t, r)$ obtained from EQMOM and TSM with $f(t, v) = f^r(t, v^{1/3})/(3v^{2/3})$. For $N = 4$, the reconstruction obtained with gamma-EQMOM is much better than when considering v-reconstruction and quite similar to the reconstruction with Ln-EQMOM, except near zero. Both are close to the exact solution, with some

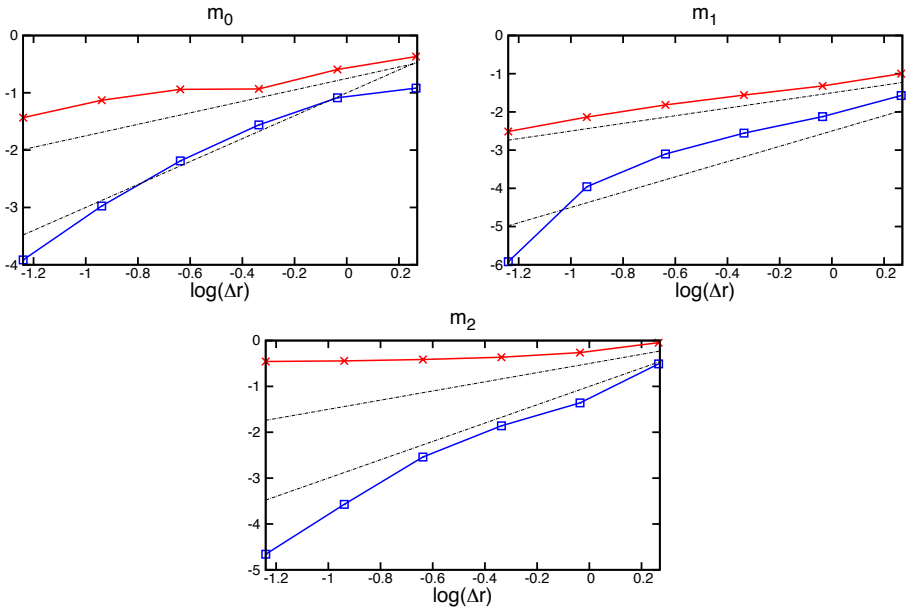

Figure 7: Error curves of moments for size reduction using OSM (red line) and TSM (blue line) with r-reconstruction. Dashed black line: order 1 and 2.

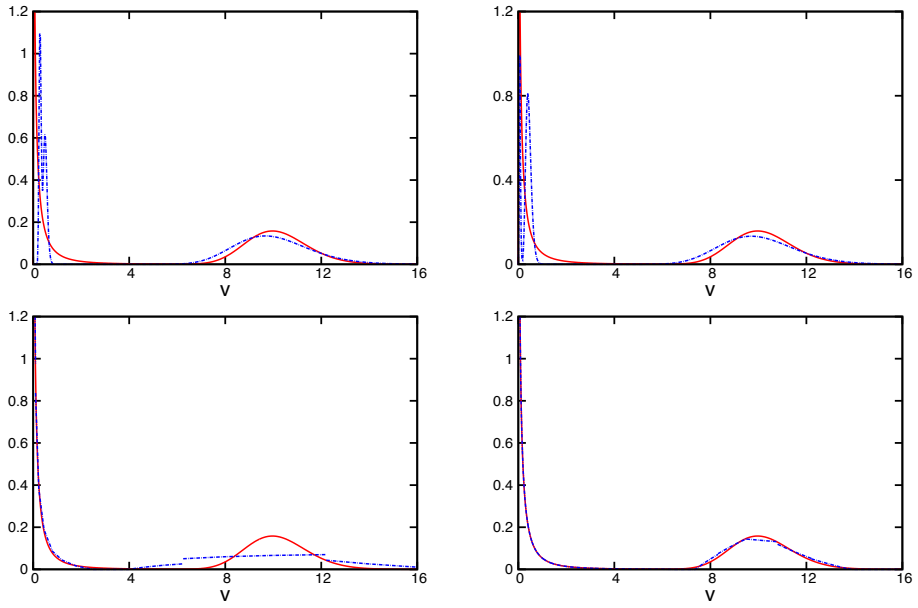

Figure 8: NDF at $t = 0.033$ for size reduction using r-reconstruction: exact (solid red line) and numerical (dashed blue line) solution. Ln-EQMOM $N = 4$ (top left). Gamma-EQMOM $N = 4$ (top right). TSM with 9 (bottom left) or 41 (bottom right) sections.

	Ln-EQMOM			gamma-EQMOM		
N	2	3	4	2	3	4
m_0	6.2×10^{-14}	1.3×10^{-13}	7.0×10^{-14}	1.3×10^{-13}	1.6×10^{-13}	8.0×10^{-14}
m_1	6.3×10^{-4}	1.3×10^{-4}	3.5×10^{-5}	4.1×10^{-4}	1.2×10^{-4}	4.1×10^{-5}
m_2	-	1.4×10^{-3}	4.3×10^{-13}	-	7.6×10^{-11}	6.4×10^{-13}
$\frac{m_1}{m_0}$	6.3×10^{-4}	1.3×10^{-4}	3.5×10^{-5}	4.1×10^{-4}	1.2×10^{-4}	4.1×10^{-5}
σ_v^2	-	1.7×10^{-3}	2.1×10^{-5}	-	9.0×10^{-5}	2.6×10^{-5}
NDF	0.36	0.34	0.34	0.42	0.42	0.43
VDF	0.25	0.26	0.30	0.38	0.41	0.47

Table 5: Normalized L^∞ norm in time of errors for diffusion-controlled growth with EQMOM using r-reconstructions.

shift for the second mode of this bimodal function. The error on this distribution and on the VDF (eliminating the singularity at zero) is indeed quite good for gamma-EQMOM (see Table 3) and also for Ln-EQMOM. When considering TSM, this error is higher than with EQMOM using $N = 4$ KDFs, except with more than 21 section and the NDF is very well reproduced with 41 sections. However, TSM is more accurate than OSM, which is not able to reproduce correctly the NDF with 82 sections, the error on the NDF and VDF being then larger than the one with gamma-EQMOM.

In summary, when considering size reduction, one can see from the examples presented in this section that gamma-EQMOM is always more accurate than Ln-EQMOM. Moreover, gamma-EQMOM gives a quite good estimate of the NDF. The convergence of EQMOM in terms of the number of moments is, however, quite slow and induces an increasing complexity of the moment space, so that considering more than nine moments (*i.e.* $N = 4$) may not be worthwhile for most applications. For better accuracy, TSM can be used, with a larger number of variables, which would have to be transported in space in many applications. However, the good convergence of TSM allows the use of a much smaller number of sections (and also of variables) than OSM for the same accuracy.

3.4. Numerical results for diffusion-controlled growth

The test case described by McGraw [40] is used here to test the schemes for diffusion-controlled growth. The initial distribution is $f^r(0, r) = ar^2 \exp(-b\, r)$ where r is the particle radius (μm), $a = 0.108\ \mu\text{m}^{-3}\text{cm}^{-3}$ and $b = 0.6\ \mu\text{m}^{-1}$. The growth rate is given by (4) with $c_{\text{gro}} = 2.34\ \mu\text{m}^2/\text{s}$ (considering $v = r^3$). Simulations are done between time 0 and $T = 20s$, with EQMOM and TSM using r-reconstruction, and OSM using a constant reconstruction in v (the method is unstable with the constant reconstruction in r). For OSM and TSM, a uniform discretization is used in the r variable, between 0 and $R_{\max} = 60\,\mu$m. Moreover, for all methods, QKS is used with a constant time step, $\Delta t = 0.01$, small enough so that the simulations are converged in time. The same kinds of post-treatments are done as with the size-reduction case, except that the NDF in r in now considered.

The normalized errors for all methods are given in Tables 5 and 6. For Ln- and gamma-EQMOM, the moment errors are very small, even with $N = 2$. One can remark that the growth model conserves the zeroth-order moment and yields closed equations for even-order r-moments. For EQMOM, the even-order r-moments are thus very accurately reproduced, *e.g.* m_2 when $N = 4$, except eventually for the last moment since it is not always well reproduced by the reconstruction. For TSM, the zeroth-order moment is also conserved, such that its error is very small and the

	OSM			TSM		
N_s	10	30	90	5	15	45
m_0	0.53	0.19	3.0×10^{-2}	3.6×10^{-14}	4.6×10^{-13}	1.9×10^{-13}
m_1	0.22	8.4×10^{-2}	2.1×10^{-2}	0.11	4.7×10^{-3}	4.7×10^{-4}
m_2	1.1	0.22	6.0×10^{-2}	0.23	1.1×10^{-2}	3.4×10^{-4}
$\frac{m_1}{m_0}$	0.87	0.17	2.6×10^{-2}	0.11	4.7×10^{-3}	4.7×10^{-4}
σ_v^2	4.7	0.68	0.14	0.54	1.2×10^{-2}	1.4×10^{-4}
NDF	0.95	0.75	0.42	1.2	0.54	0.19
VDF	1.1	0.53	0.19	0.67	0.29	6.9×10^{-2}

Table 6: Normalized L^∞ norm in time of errors for diffusion-controlled growth with TSM using r-reconstructions.

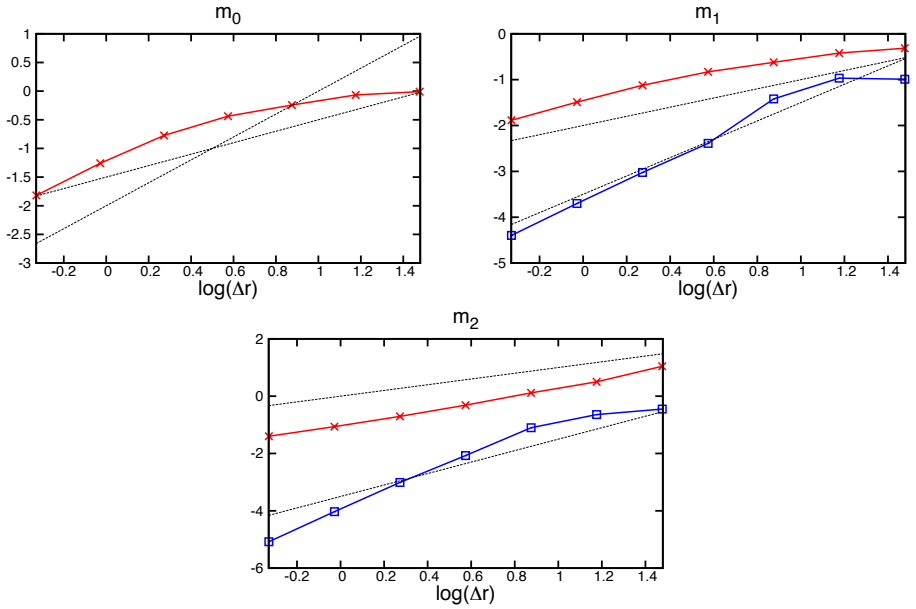

Figure 9: Error curves of moments for diffusion-controlled growth using OSM (red line) and TSM (blue line) reconstructions. Dashed black line: order 1 and 2.

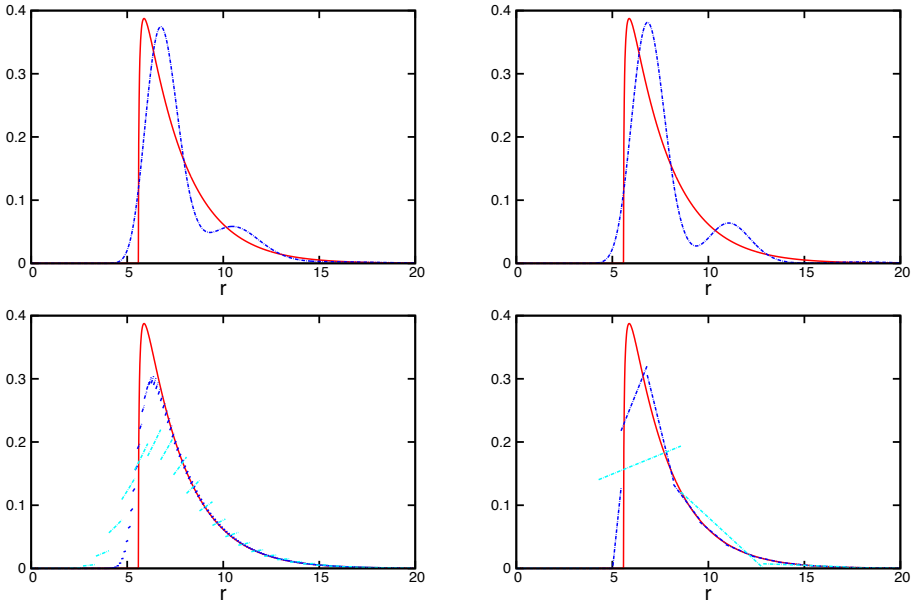

Figure 10: NDF for diffusion-controlled growth at $t = 20$: numerical (dashed blue line) vs. exact (solid red line). EQMOM reconstruction with r-moments, $N = 4$: Ln (top left), gamma (top right). OSM reconstruction (bottom left) with 90 (dashed cyan line) and 500 (dashed blue line) sections. TSM reconstruction (bottom right) with 15 (dashed cyan line) and 45 (dashed blue line) sections.

accuracy of the moments of orders 1 and 2 is high, even with only 15 sections. For OSM, a large number of sections is needed to reproduce the moments (even at zero order, which is not conserved) with an error of a few percent. The error curves for the moments found with OSM and TSM are shown in Fig. 9 as functions of the section size, using 3 to 129 sections. It can be clearly observed that the convergence rates are at least first and second order, respectively, for OSM and TSM.

Results for the reconstructed NDFs at time T are shown in Fig. 10. As can be observed, the EQMOM results are very similar for Ln- and gamma-EQMOM, and in relatively good agreement with the exact solution. The errors on the NDF and VDF (see Table 5) do not really depend on the number of KDFs and are about 30 or 40 %. On the other hand, the OSM result does not capture correctly the sharp jump in NDF at $r \approx 5.5$, except with a very large number of sections (*e.g.* 500). In contrast, TSM with 45 sections does a good job of reproducing the exact NDF.

In summary, when considering surface growth, one can see from the examples presented in this section that gamma- and Ln-EQMOM give equivalent results, which are very good for the moments and relatively good for the NDF, and not significantly improved using a larger number of moments. Discretized methods, especially OSM, are disfavored by the fact that the NDF is shifted toward the larger sizes and by the sharp jump of the exact NDF. However, TSM is able to reproduce well moments and the sharp NDF with a quite small number of sections, much smaller than for OSM.

4. Aggregation

In this section we apply EQMOM and the discretized methods to solve a PBE with only aggregation. Such applications are known to be particularly challenging for discretized methods because the mean particle size and variance grow continuously with time. From a numerical perspective, the aggregation operator has an integro-differential form that strongly couples all points in size phase space. In real applications, numerical simulation of the aggregation term is often the most computationally expensive operation.

4.1. EQMOM

As first shown by Marchisio et al. [39], QBMM are particularly well suited for aggregation because the abscissas evolve in phase space to adapt to the changing shape of the NDF. After using the EQMOM moment-inversion algorithm, we obtain a closure for (5) and (6). Solving these moment equations requires the numerical approximation of the integrals in (6) since the KDF $\delta_\sigma(\xi,\xi_\alpha)$ is a smooth function. This can be done by using the quadrature specific to each KDF:

$$\int_0^\infty g(v)\,\delta_\sigma(\xi,\xi_\alpha)\,\mathrm{d}v \approx \sum_{\beta=1}^{N_\alpha} \omega_{\alpha\beta}\,g(v_{\alpha\beta}) \tag{44}$$

where N_α is the number of secondary quadrature points. N_α must be larger than N (in practice $N_\alpha = N+1$), in such a way that (44) is exact when g is a polynomial of degree less than or equal to $2N$. These weights $\omega_{\alpha\beta}$ and abscissas $v_{\alpha\beta}$ can be easily computed from the known recurrence coefficients of the orthogonal polynomials corresponding to the KDF: the generalized Laguerre [61] and Stieltjes-Wigert [69] for gamma- and Ln-EQMOM, respectively. The approximation of the integral for any arbitrary function with respect to the reconstructed NDF is then

$$\int_0^\infty g(v)\,f(v)\,\mathrm{d}v = \sum_{\alpha=1}^{N}\sum_{\beta=1}^{N_\alpha} w_{\alpha\beta}\,g(v_{\alpha\beta}) \tag{45}$$

where $w_{\alpha\beta} = w_\alpha\,\omega_{\alpha\beta}$. Finally, we obtain the system of moment equations for aggregation, for $k\in\mathbb{N}$:

$$\frac{dm_k}{dt} = \frac{1}{2}\sum_{\alpha_1=1}^{N}\sum_{\beta_1=1}^{N_{\alpha_1}}\sum_{\alpha_2=1}^{N}\sum_{\beta_2=1}^{N_{\alpha_2}} w_{\alpha_1\beta_1}w_{\alpha_2\beta_2}\left[(v_{\alpha_1\beta_1}+v_{\alpha_2\beta_2})^k - v_{\alpha_1\beta_1}^k - v_{\alpha_2\beta_2}^k\right]\beta(v_{\alpha_1\beta_1},v_{\alpha_2\beta_2}) \tag{46}$$

A realizable ODE solver must be used to solve this system.

4.2. TSM

The equations for the moments in one section $[V_{\min},V_{\max}] = [V_{k-1},V_k]$ are given by (5) and (6). For aggregation, the integration domain $\Omega_k = \{(v^*,v') > 0 / V_{k-1} < v^*+v' < V_k\}$ then appears. Since the closure consists in a reconstruction of the NDF on each section, this domain is divided into some elementary sub-domains: $\mathcal{D}_{ijk} = \Omega_k \cap ([V_{i-1},V_i]\times[V_{j-1},V_j])$ [59]. One then defines the following elementary integrals:

$$\begin{pmatrix} Q^n_{ijk} \\ Q^*_{ijk} \end{pmatrix} = \iint_{\mathcal{D}_{ijk}} \begin{pmatrix} 1 \\ v^* \end{pmatrix} \beta(v^*,v')\,f(v^*)\,f(v')\,\mathrm{d}v^*\,\mathrm{d}v', \tag{47}$$

The equations for the moments of orders zero and one in v in section k are then

$$\partial_t N_k = \frac{1}{2}\sum_{i=1}^{N_s}\sum_{j=1}^{N_s} Q^n_{ijk} - \sum_{i=1}^{N_s}\sum_{j=1}^{N_s} Q^n_{kij} \tag{48a}$$

$$\partial_t M_k = \sum_{i=1}^{N_s}\sum_{j=1}^{N_s} Q^*_{ijk} - \sum_{i=1}^{N_s}\sum_{j=1}^{N_s} Q^*_{kij} \tag{48b}$$

The elementary integrals are computed using a 5-point Gauss-Legendre quadrature in the variable r, in each direction. Let us also remark that in the case of a time-independent collision kernels, a numerically efficient way to compute the source terms can be developed [29], as for the sectional method in the spray context [25], using pre-computation of some terms and a compact storage of the variables. Finally, as for QBMM, the realizability constraint has to be respected in the resolution of this ODE system.

4.3. Realizable, adaptive time step

Due to the complexity of aggregation kernels in practical problems [2], the ODE system can be stiff and we then want to use an adaptive time step to limit the cost of the computations. Concerning realizability, since the aggregation operator does not move the moment vector to the boundary of moment space, explicit Euler methods with small enough time steps can be used as well as any convex combination of Euler explicit time steps, such as the strong-stability-preserving (SSP), explicit Runge-Kutta methods [70]. We therefore use an adaptive time-step algorithm, based on embedded SSP explicit Runge-Kutta methods, with a time-step selection designed both to control the error and to ensure the realizability of the moment set (see Appendix C for details).

4.4. Numerical results

We present results in this section for two aggregation test cases from [49] (cases 9 and 11). First, the sum kernel $\beta(v,v') = v + v'$ is used with initial condition $f(0,v) = \exp(-v)$. An analytical NDF for this problem is given in [71]. Then, the more complex Brownian kernel: $\beta(v,v') = \left(v^{-1/3} + v'^{-1/3}\right)\left(v^{1/3} + v'^{1/3}\right)$ is used with the same initial condition. In this case, a self-similar NDF is found for large enough time [72]. For TSM, we consider the following geometric discretization:

$$V_0 = 0, \qquad V_k = \frac{V_{\max}}{(\mathsf{R}N_s)^{\frac{N_s-k+1}{N_s-1}}}, \quad k \in \{1,\dots,N_s-1\}, \qquad V_{N_s} = \infty \tag{49}$$

where R is a user-defined parameter, as well as $V_{\max}$: here, $V_{\max} = 25000$ and $\mathsf{R} = 5000$. The same kind of discretization is used for OSM, without the last section and then with a larger value for $V_{\max}$ ($V_{\max} = 30000$, $\mathsf{R} = 10^4$). A dependence on the number of sections is then introduced in the ratio between two successive section sizes, $(\mathsf{R}N_s)^{\frac{1}{N_s-1}}$, in such a way that the discretization tends to a uniform discretization when N_s tends to infinity.

Aggregation with the sum kernel yields quantitatively similar results for r- and v-moments. In general, the results found with v-reconstruction are slightly more accurate, but since the r variable gives better accuracy for other phenomena (*e.g.* size reduction), all results presented here are obtained using r-reconstruction. The normalized errors are given in Tables 7 and 8. For the moments, EQMOM yields very small errors for both KDFs, even with $N = 2$. These results are

	Ln-EQMOM			gamma-EQMOM		
N	2	3	4	2	3	4
m_0	4.5×10^{-7}	1.1×10^{-7}	3.3×10^{-8}	4.7×10^{-7}	1.2×10^{-7}	3.3×10^{-8}
m_2	–	1.8×10^{-6}	5.1×10^{-7}	–	1.9×10^{-6}	5.2×10^{-7}
$\frac{m_1}{m_0}$	4.5×10^{-7}	1.1×10^{-7}	3.3×10^{-8}	4.7×10^{-7}	1.2×10^{-7}	3.3×10^{-8}
σ_v^2	–	1.7×10^{-6}	5.0×10^{-7}	–	1.8×10^{-6}	5.0×10^{-7}
NDF	0.22	0.36	0.66	0.25	0.18	0.12
VDF	0.17	0.20	0.27	0.36	0.27	0.20

Table 7: Aggregation with the sum kernel: L^∞ norm in time of relative errors with EQMOM using r-reconstruction.

	OSM			TSM		
N_s	10	30	90	5	15	45
m_0	0.25	0.13	5.3×10^{-2}	1.7×10^{-3}	4.5×10^{-3}	6.3×10^{-3}
m_2	1.5×10^{3}	31	0.26	0.73	0.13	2.4×10^{-3}
$\frac{m_1}{m_0}$	0.20	0.12	5.0×10^{-2}	1.7×10^{-3}	4.5×10^{-3}	6.3×10^{-3}
σ_v^2	1.4×10^{3}	29	0.22	0.75	0.13	3.7×10^{-3}
NDF	0.55	0.22	8.4×10^{-2}	0.32	2.7×10^{-2}	1.5×10^{-2}
VDF	0.94	0.37	8.3×10^{-2}	0.79	9.1×10^{-2}	1.1×10^{-2}

Table 8: Aggregation with the sum kernel: L^∞ norm in time of relative errors with OSM and TSM using r-reconstruction.

consistent with previous work using QBMM [39, 49] and are due to the fact that for the sum kernel, the equations on the moments are closed, except for the last one. In comparison, for OSM and TSM the errors on the moments are significantly larger than with EQMOM. This difference is mainly due to the nature of aggregation where the NDF moves to larger and larger r as time progresses (if it is not in competition with size-reduction phenomena, as it might be in some applications). With QBMM, the abscissas follow the movement of the NDF in phase space, while for discretized methods the discretization of phase space is fixed and the value of $V_{\max}$ has to be adapted to the final time. Nevertheless, for finite times, TSM with as few as 15 sections provides a much more accurate reconstruction of the NDF as compared to EQMOM.

For Brownian aggregation, the time evolutions of selected moments are shown in Fig. 11, and the NDFs at $t = 10$ are given in Fig. 12. For the moments, EQMOM with either KDF yields very accurate predictions (not shown), confirming previous observations [39]. OSM converges to the reference solution after approximately 90 sections, while TSM gives accurate predictions with as few as 15 sections. With a small number of sections, OSM tends to over-predict the variance σ_v^2 by a large amount. This is due to the behavior of the reconstructed NDF in the largest sections, which for OSM decays too slowly with increasing v. For this reason, the errors in moments of orders greater than two are significant, making OSM unsuitable for aggregation processes. The reconstructed NDFs in Fig. 12 confirm the general trend that gamma-EQMOM yields better results than Ln-EQMOM. The NDF found with gamma-EQMOM is quite accurate, as previously reported [49]. In order to obtain a comparable NDF with OSM at least 30 sections are required, while for TSM 15 sections yield an accurate NDF.

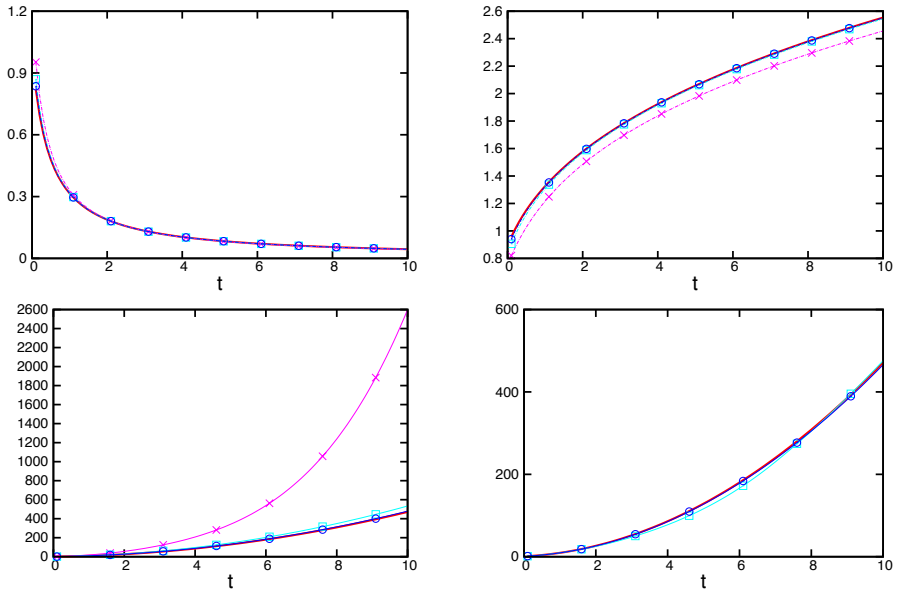

Figure 11: Brownian aggregation with self-similar NDF. Evolution of m_0 (top left), mean particle diameter (top right) and variance (bottom) versus reference solution (red solid line). OSM (top, bottom left) with 10 (dashed magenta line), 30 (dashed cyan line) and 90 (dashed blue line) sections. TSM (bottom right) with 5 (dashed cyan line), and 15 (dashed blue line) sections.

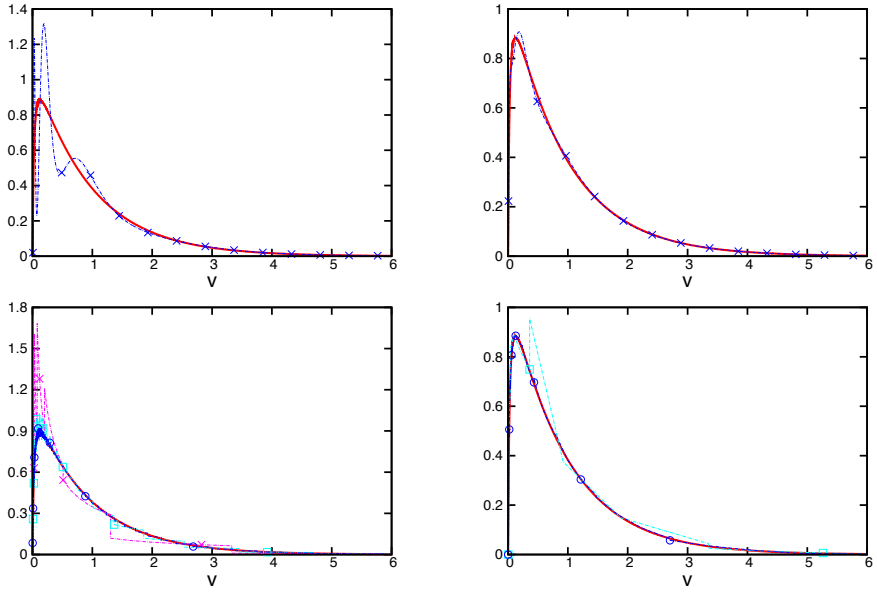

Figure 12: Brownian aggregation with self-similar NDF (red solid line). Ln-EQMOM (top left): $N = 4$ (dashed blue line). Gamma-EQMOM (top right): $N = 4$ (dashed blue line). OSM (bottom left) with 10 (dashed magenta line), 30 (dashed cyan line) and 90 (dashed blue line) sections. TSM (bottom right) with 5 (dashed cyan line), and 15 (dashed blue line) sections.

5. Operator time-splitting method for general problems

5.1. Strang time-splitting method

We consider in this section an algorithm to solve moment equations with all the types of source terms appearing in fine-particle applications. The idea is to use an operator time-splitting method that solves successively in one time step the nucleation-aggregation and particle-size-change operators. In this work, we use the Strang time-splitting method [73], which is second order in time: we solve successively, in one time step $\Delta t = t_{n+1} - t_n$,

1. the nucleation-aggregation operator on $\left[t_n, t_n + \frac{\Delta t}{2}\right]$
2. the particle-size-change operator on $[t_n, t_{n+1}]$
3. the nucleation-aggregation operator on $\left[t_n + \frac{\Delta t}{2}, t_{n+1}\right]$

Since the nucleation-aggregation operator is stiffer than the particle-size-change operator, in general, the splitting time step Δt is chosen to satisfy the stability of the latter. Then, we apply an adaptive time step for the nucleation-aggregation operator. For each operator, we use the realizable and robust schemes given in Secs. 3 and 4 for particle-size-change and nucleation-aggregation processes, respectively.

5.2. Numerical results

We investigate here a test case with nucleation, aggregation and size reduction where the nuclei size is $V_{\text{nuc}} = 1$ and the nucleation rate is $j(t) = 10^3 \, \mathbb{1}_{[0,0.5]}(t)$. The Brownian kernel is used for aggregation, and the size-reduction rate is given by (3) with $c_{\text{red}} = 3$. For this test case, a large number of nuclei are produced at the start, leading to significant particle growth due to aggregation. Eventually, growth is moderated by size reduction, resulting in a maximum in time of the mean particle diameter $m_{1/3}/m_0$. For sufficiently long times, size reduction would consume all particles. Here, we show results only up to the time where size reduction begins to overtake aggregation ($t \approx 6$).

For TSM, we use the following geometric discretization, similar to the one classically used for soot applications with the sectional method:

$$V_k = \bar{V} \left(\frac{V_{\max}}{\bar{V}} \right)^{\frac{k-1}{N_s - 2}}, \quad k \in \{1, \ldots, N_s - 1\}, \tag{50}$$

with $V_0 = 0$ and $V_{N_s} = \infty$. The volume $\bar{V}$ is slightly larger than the nuclei size ($\bar{V} = 1.001$) and $V_{\max} = 10^4$. For OSM, the last section is skipped, $V_{\max} = 2 \times 10^4$ and the first section is divided in two sections ($N_s = 10$) or three ($N_s = 30$) or seven ($N_s = 90$) where the last one ([0.95 1.05], $\bar{V} = 1.05$) contains the nuclei size. All simulations are done with a constant splitting time step $\Delta t = 0.003$. A reference solution is also computed, using TSM with 101 sections and a ten time smaller splitting time step.

Except for OSM, all methods yield essentially the same results for m_0 and the mean particle diameter as seen in Fig. 13. With OSM, the mean particle diameter during the nucleation period ($t < 0.5$) is under-predicted and m_0 is over-predicted even when a relatively large number of sections is used. For the variance σ_v^2, the EQMOM results for $N = 3$ and 4 are essentially identical, and equal to the TSM result found with 101 sections (see Fig. 14). In contrast, OSM converges slowly towards the reference solution with increasing numbers of sections, while TSM requires approximately 45 sections to attain convergence. As seen in Fig. 15, the reconstructed NDFs differ significantly

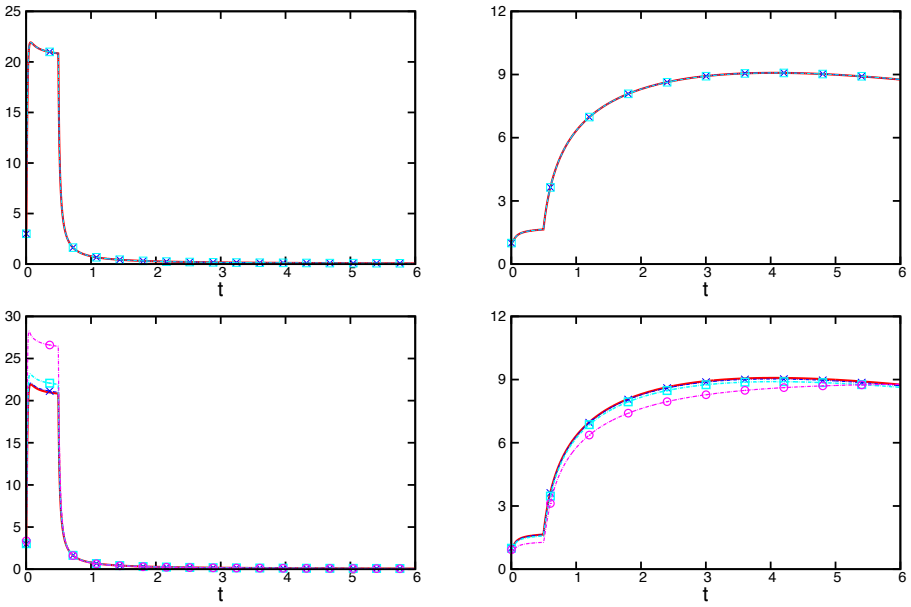

Figure 13: Time evolution of m_0 (left) and mean particle diameter (right). Ln-EQMOM (top row): $N = 3$ (dashed cyan line), $N = 4$ (dashed blue line). OSM (bottom row): 10 (dashed magenta line), 30 (dashed cyan line), 90 (dashed blue line) sections. TSM, with 101 sections: (red solid line).

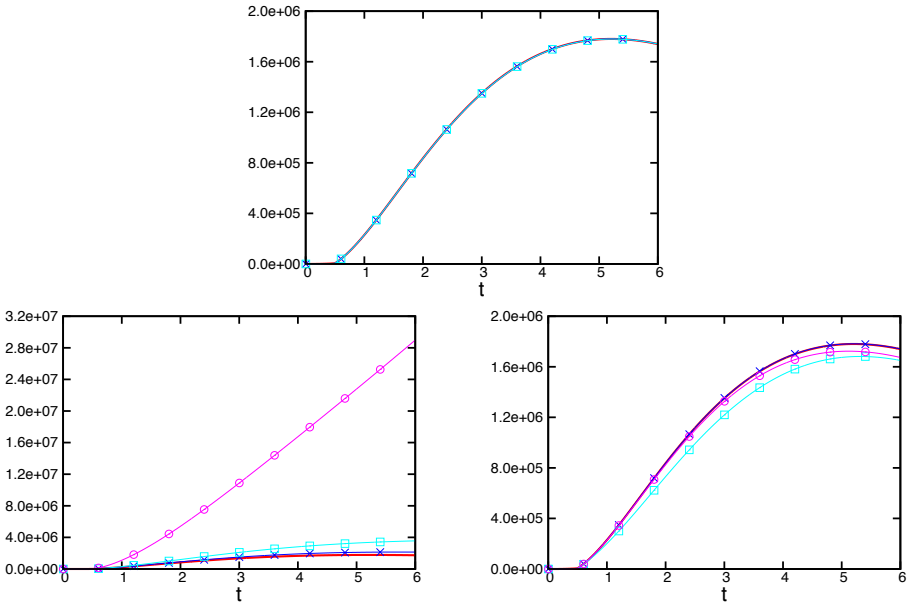

Figure 14: Time evolution of σ_v^2. Gamma-EQMOM (top): $N = 3$ (dashed cyan line), $N = 4$ (dashed blue line). OSM (bottom left): 10 (dashed magenta line), 30 (dashed cyan line), 90 (dashed blue line) sections. TSM (bottom right): 5 (dashed cyan line), 15 (dashed magenta line), 45 (dashed blue line), 101 (red solid line).

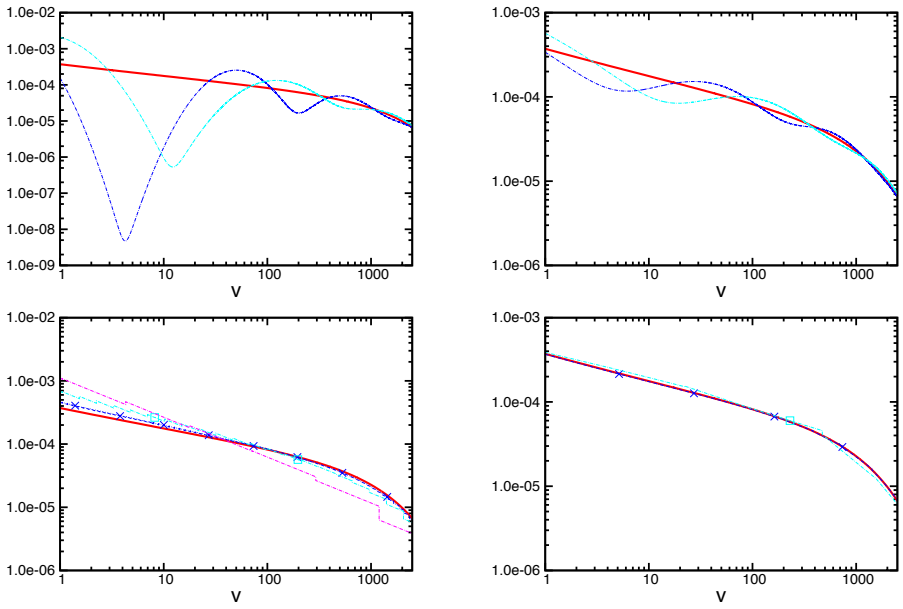

Figure 15: Reconstructed NDF at $t = 6$. Ln-EQMOM (left): $N = 3$ (dashed cyan line) and $N = 4$ (dashed blue line). Gamma-EQMOM (right): $N = 3$ (dashed cyan line) and $N = 4$ (dashed blue line). OSM (bottom left): 10 (dashed magenta line), 30 (dashed cyan line), 90 (dashed blue line) sections. TSM (bottom right): 5 (dashed cyan line), 15 (dashed magenta line), 45 (dashed blue line), 101 (red solid line).

between the methods. In general, Ln-EQMOM has more obvious modal peaks as compared to gamma-EQMOM, which are associated with the behavior of the KDFs at $v = 0$. Increasing N from 3 to 4 KDFs shows some improvement (especially for gamma-EQMOM), but the convergence is slow. In contrast, TSM yields a better NDF reconstruction as compared to EQMOM, even with as few as 5 sections, while OSM requires a much larger number of sections to obtain reasonably accurate results.

6. Conclusions

In this work, we have developed quadrature-based moment methods (EQMOM with gamma and log-normal KDF) and a hybrid method (TSM) for modeling fine particles undergoing nucleation, aggregation and continuous changes (growth and size reduction). For both classes of methods, efficient algorithms are given to reconstruct the NDF, using analytical formula for TSM and an improved algorithm compared to [49] for EQMOM, which are able to deal with the boundary of moment space. In addition, realizable numerical schemes are presented for each individual term in the PBE, as well as an operator-splitting approach to resolve the complete problem.

In the test cases considered, for EQMOM the gamma KDF leads to more accurate results than the log-normal KDF. Moreover, better results are obtained using fractional (r) moments. For example, more accurate results are found for cases with size reduction and the results for aggregation are not significantly different with fractional moments. Consistent with previous results in the literature [1, 39], we find that EQMOM is well suited for accurately predicting the evolution of the moments for general problems, especially when aggregation processes are involved. Furthermore, EQMOM with $N = 4$ predicts the NDF with a reasonably good accuracy.

We also showed that the hybrid TSM method is much more accurate than the widely used sectional method. Indeed, TSM conserves both the global number and mass of the particles, and can deal with a semi-infinite support of the NDF, even if the size-space discretization must be adapted to the expected range of particle sizes for good accuracy. Because the NDF reconstruction found with TSM is much better in each section, the number of sections needed to obtain good accuracy for the first few moments and the NDF is much smaller as compared to OSM. In general, discretized methods are usually not as efficient as EQMOM for predicting the moments, but TSM is able to accurately predict the NDF with a reasonably small number of sections. In contrast, EQMOM converges slowly to the exact NDF as the number of moments increases and can not deal with too large a number of moments due to the increasing complexity of moment space and the numerical accuracy of the Chebyshev algorithm.

Further studies are needed to extend the accurate and realizable numerical schemes presented here to multivariate PBE models for fine-particle formation [4, 8, 74]. This can be accomplished by conditioning the other internal variable by the volume, using the mono-kinetic assumption, along the lines of what has been done with the size-velocity internal variables for sprays [24, 25, 46, 29] and bubbly flows [2, 75, 76]. Another very important topic for fine-particle applications involving spatial transport of the moments is the development of realizable, high-order advection [55, 47] and diffusion [56] schemes, which can be coupled with a Navier-Stokes solver for the carrier fluid. Ideally, such schemes should accommodate unstructured computational grids and both explicit and implicit time stepping.

Acknowledgments

This work was supported by a grant from French National Research Agency: ASMAPE project (ANR-13-TDMO-02 ASMAPE, PI IFPen: O. Colin; PI for EM2C Lab.: F. Laurent).

Appendix A. Change of variable in the PBE for spherical particles

In this work, the chosen size variable is volume v, which is then the internal variable of the NDF: $f(t,v)$. However, for spherical particles, the radius $r = \left(\frac{3v}{4\pi}\right)^{1/3}$ can be equivalently used. Since the corresponding NDF f^r represents the same particle population, one has $f(t,v)\mathrm{d}v = f^r(t,r)\mathrm{d}r$, and thus

$$f^r(t,r) = 4\pi r^2 \, f\left(t, \frac{4\pi}{3} r^3\right). \tag{A.1}$$

While the change of variable is easy for most of the terms in the PBE, the drift terms are written $\partial_\xi[\mathcal{R}_\xi(t,\xi)\, f(t,\xi)]$ with ξ being radius or volume. Since $\mathcal{R}_\xi(t,\xi)$ represents the rate of change $\frac{\mathrm{d}\xi}{\mathrm{d}t}$ for the size ξ, one has

$$\mathcal{R}_r(t,r) 4\pi r^2 = \mathcal{R}_v\left(t, \frac{4\pi}{3} r^3\right). \tag{A.2}$$

For example, if $\mathcal{R}_r(t,r) = c(t)/r$ (*e.g.* diffusion-controlled growth), then $\mathcal{R}_v(t,v) = 3^{1/3}(4\pi)^{2/3} c(t) v^{1/3}$. Note that for simplicity $\mathcal{R}_v$ is denoted $\mathcal{R}$ in the rest of the paper.

Appendix B. ζ–Chebyshev algorithm

In order to compute the coefficients $\{\zeta_k\}_{k\in\mathbb{N}^*}$ from the moments $\{m_k\}_{k\in\mathbb{N}}$, the Chebyshev algorithm is used, combined to formula (10). Then, setting $\sigma_{0,k} = m_k$ for $k \geq 0$, $a_0 = m_1/m_0$ and $\zeta_1 = a_0$, one computes, for $l \geq 1$:

$$\sigma_{1,l} = \sigma_{0,l+1} - a_0 \sigma_{0,l}.$$

For $k \geq 1$, one then computes successively:

$$b_k = \frac{\sigma_{k,k}}{\sigma_{k-1,k-1}}\,, \qquad \zeta_{2k} = \frac{b_k}{\zeta_{2k-1}} \tag{B.1}$$

$$a_k = \frac{\sigma_{k,k+1}}{\sigma_{k,k}} - \frac{\sigma_{k-1,k}}{\sigma_{k-1,k-1}}\,, \qquad \zeta_{2k+1} = a_k - \zeta_{2k} \tag{B.2}$$

$$\sigma_{k+1,l} = \sigma_{k,l+1} - a_k \sigma_{k,l} - b_k \sigma_{k-1,l}\,, \qquad l \geq k+1 \tag{B.3}$$

Appendix C. Realizable, adaptive time-step algorithm

Let us consider the system of ODEs arising from solving the moment equations:

$$\frac{dy(t)}{dt} = f(t, y(t)) \tag{C.1}$$

where $t \in \mathbb{R}^+$, $y, f \in \mathbb{R}^d$. Explicit Runge-Kutta methods (ERK) [70, 77, 78, 79] are used to solve this equation: from the approximate solution $y^{(n)}$ at time t_n, the solution at time $t_{n+1} = t_n + h$ is approximated by

$$y^{(n+1)} = y^{(n)} + h \sum_{i=1}^{s} b_i f(\tau_i, \eta_i) \tag{C.2}$$

where s is the number of stages of the ERK method, τ_i and η_i are given by

$$\tau_i = t_n + c_i h \tag{C.3a}$$

$$\eta_i = y^{(n)} + h \sum_{j=1}^{i-1} a_{ij} f(\tau_j, \eta_j) \tag{C.3b}$$

and the coefficients b_i, a_{ij}, c_i are given by Butcher tables [77, 78, 79].

An adaptive time-step method can be obtained with an embedded-explicit Runge-Kutta method (EERK) [77, 78, 79]. Then, two ERK methods are considered, using the same auxiliary values η_i, but with a different linear combination of these values so that one is p^{th}-order accurate and the other $(p+1)^{\text{th}}$-order accurate. This provides an error estimate. The method can be written in the form of a combined Butcher table:

0					
c_2	a_{21}				
c_3	a_{31}	a_{32}			
$\vdots$	$\vdots$	$\vdots$	$\ddots$		
c_s	a_{s1}	a_{s2}	$\dots$	$a_{s,s-1}$	
	b_1	b_2	$\dots$	b_{s-1}	b_s
	b'_1	b'_2	$\dots$	b'_{s-1}	b'_s

where the two last lines stand for ERK of order p and $p+1$, respectively, and the solutions read

$$y^{(n+1)} = y^{(n)} + h \sum_{i=1}^{s'} b_i f(\tau_i, \eta_i) \tag{C.4a}$$

$$\hat{y}^{(n+1)} = y^{(n)} + h \sum_{i=1}^{s} b'_i f(\tau_i, \eta_i) \tag{C.4b}$$

where $s' = s$ or $s' = s - 1$. In this work, we use strong stability preserving (SSP) Runge-Kutta methods [70]: one of order-two embedded in the optimal third-order SSP Runge-Kutta method. The coefficients are given by

0			
1	1		
$1/2$	$1/4$	$1/4$	
	$1/2$	$1/2$	
	$1/6$	$1/6$	$2/3$

Owing to the fact that SSP Runge-Kutta yields a convex combination of some explicit Euler steps, we are able to ensure the realizability of the final moment set by checking each of the intermediate sets and adjusting the time step such that they are realizable. The parameter *ierr* (see Fig. C.16) is set to $ierr = 0$ when the corresponding intermediate moment sets are realizable.

The local error estimate reads

$$\epsilon = \|y^{(n)} - \hat{y}^{(n)}\| = \frac{h}{3} \|f(\tau_1, \eta_1) + f(\tau_2, \eta_2) - 2f(\tau_3, \eta_3)\| \tag{C.5}$$

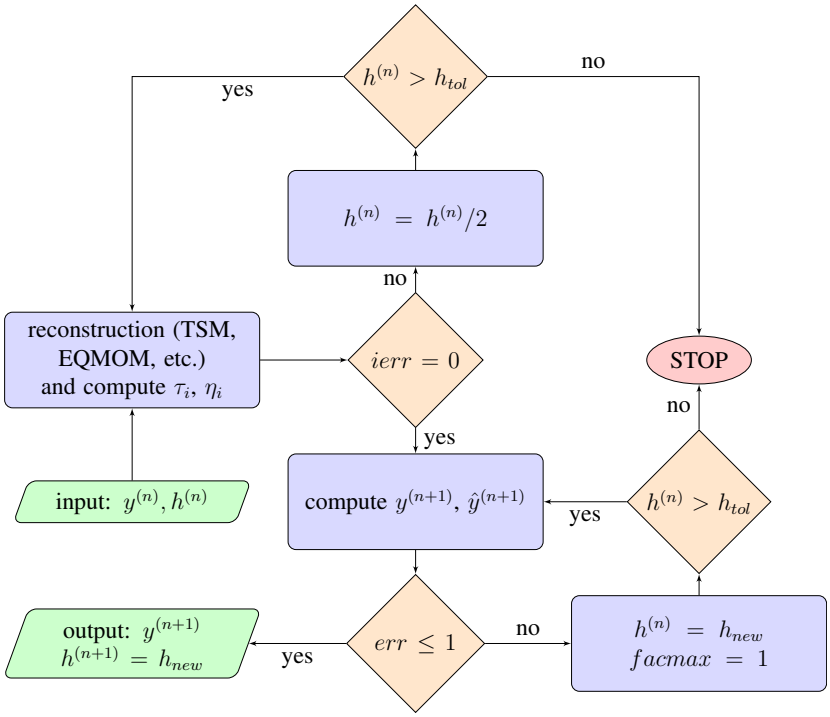

Figure C.16: Realizable, adaptive time-step algorithm.

We want this error to satisfy component-wise

$$|y_i^{(n)} - \hat{y}_i^{(n)}| \leq sc_i, \qquad sc_i = Atol_i + \max\left(|y_i^{(n-1)}|, |y_i^{(n)}|\right) Rtol_i \tag{C.6}$$

where $Atol_i$ and $Rtol_i$ are, respectively, user-defined absolute and relative tolerances. As a measure of the error we take

$$err = \sqrt{\frac{1}{n}\sum_{i=1}^{d}\left(\frac{y_i^{(n)} - \hat{y}_i^{(n)}}{sc_i}\right)^2} \tag{C.7}$$

Then err is compared to 1 to find an "optimal" step size:

$$h_{new} = h \min\left\{facmax, \max\left[facmin, \frac{fac}{err^{1/(p+1)}}\right]\right\}. \tag{C.8}$$

The algorithm for the realizable, adaptive time step is shown in Fig. C.16.

References

[1] D. L. Marchisio, J. T. Pikturna, R. O. Fox, R. D. Vigil, A. A. Barresi, Quadrature method of moments for population–balance equations, AIChE Journal 49 (5) (2003) 1266–1276.

[2] D. L. Marchisio, R. O. Fox, Computational Models for Polydisperse Particulate and Multiphase Systems, Cambridge University Press, Cambridge, UK, 2013.

[3] D. Piton, R. O. Fox, B. Marcant, Simulation of fine particle formation by precipitation using computational fluid dynamics, The Canadian Journal of Chemical Engineering 78 (5) (2000) 983–993.

[4] V. Raman, R. O. Fox, Modeling of fine-particle formation in turbulent flames, Annual Review of Fluid Mechanics 48 (2016) 159–190.

[5] D. Ramkrishna, M. R. Singh, Population balance modeling: Current status and future prospects, Annual Review of Chemical and Biomolecular Engineering 5 (2014) 123–46.

[6] S. Rigopoulos, Population balance modelling of polydispersed particles in reactive flows, Progress in Energy and Combustion Science 36 (2010) 412–443.

[7] F. Sporleder, Z. Borka, J. Solsvik, H. A. Jakobsen, On the population balance equation, Reviews in Chemical Engineering 28 (2012) 149–169.

[8] Y. Sung, V. Raman, H. Koo, M. Mehta, R. O. Fox, Large-eddy simulation modeling of turbulent flame synthesis of titania nanoparticles using a bivariate particle description, AIChE Journal 60 (2) (2014) 459–472.

[9] L. Wang, R. O. Fox, Application of in situ adaptive tabulation to CFD simulation of nanoparticle formation by reactive precipitation, Chemical Engineering Science 58 (19) (2003) 4387–4401.

[10] A. Zucca, D. L. Marchisio, A. A. Barresi, R. O. Fox, Implementation of the population balance equation in CFD codes for modelling soot formation in turbulent flames, Chemical Engineering Science 61 (1) (2006) 87–95.

[11] S. Kumar, D. Ramkrishna, On the solution of population balance equations by discretization–i. a fixed pivot technique, Chemical Engineering Science 51 (8) (1996) 1311–1332.

[12] M. Vanni, Approximate population balance equations for aggregation–breakage processes, Journal of Colloid and Interface Science 221 (2) (2000) 143–160.

[13] R. Kumar, J. Kumar, G. Warnecke, Convergence analysis of a finite volume scheme for solving non-linear aggregation-breakage population balance equations, Kinet. Relat. Models 7 (4) (2014) 713–737.

[14] J. Kumar, M. Peglow, G. Warnecke, S. Heinrich, L. Mörl, Improved accuracy and convergence of discretized population balance for aggregation: The cell average technique, Chemical Engineering Science 61 (10) (2006) 3327–3342.

[15] S. Kumar, D. Ramkrishna, On the solution of population balance equations by discretization–iii. nucleation, growth and aggregation of particles, Chemical Engineering Science 52 (24) (1997) 4659–4679.

[16] F. Filbet, P. Laurençot, Numerical simulation of the Smoluchowski coagulation equation, SIAM J. Sci. Comput. 25 (6) (2004) 2004–2028.

[17] J.-P. Bourgade, F. Filbet, Convergence of a finite volume scheme for coagulation-fragmentation equations, Math. Comp. 77 (262) (2008) 851–882.

[18] S. Qamar, G. Warnecke, M. P. Elsner, On the solution of population balances for nucleation, growth, aggregation and breakage processes, Chemical Engineering Science 64 (9) (2009) 2088–2095.

[19] R. Kumar, J. Kumar, G. Warnecke, Moment preserving finite volume schemes for solving population balance equations incorporating aggregation, breakage, growth and source terms, Math. Models Methods Appl. Sci. 23 (7) (2013) 1235–1273.

[20] J. Kumar, G. Warnecke, Convergence analysis of sectional methods for solving breakage population balance equations. I. The fixed pivot technique, Numer. Math. 111 (1) (2008) 81–108.

[21] J. Kumar, G. Warnecke, Convergence analysis of sectional methods for solving breakage population balance equations. II. The cell average technique, Numer. Math. 110 (4) (2008) 539–559.

[22] A. K. Giri, E. Hausenblas, Convergence analysis of sectional methods for solving aggregation population balance equations: the fixed pivot technique, Nonlinear Anal. Real World Appl. 14 (6) (2013) 2068–2090.

[23] F. Gelbard, Y. Tambour, J. H. Seinfeld, Sectional representations for simulating aerosol dynamics, Journal of Colloid and Interface Science 76 (2) (1980) 541–556.

[24] F. Laurent, M. Massot, Multi-fluid modelling of laminar polydisperse spray flames: origin, assumptions and comparison of sectional and sampling methods, Combustion Theory and Modelling 5 (2001) 537–572.

[25] F. Laurent, M. Massot, P. Villedieu, Eulerian multi-fluid modeling for the numerical simulation of coalescence in polydisperse dense liquid sprays, J. Comput. Phys. 194 (2) (2004) 505–543.

[26] K. Netzell, H. Lehtiniemi, F. Mauss, Calculating the soot particle size distribution function in turbulent diffusion flames using a sectional method, Proceedings of Combustion Institute 31 (2007) 677–674.

[27] D. Aubagnac-Karkar, Sectional soot modeling for diesel RANS simulations, Ph.D. thesis, Ecole Centrale Paris, available online at https://tel.archives-ouvertes.fr/tel-01132323 (2014).

[28] F. Laurent, Numerical analysis of Eulerian multi-fluid models in the context of kinetic formulations for dilute evaporating sprays, M2AN Math. Model. Numer. Anal. 40 (3) (2006) 431–468.

[29] F. Laurent, A. Sibra, F. Doisneau, Two-size moment multi-fluid model: a robust and high-fidelity description of polydisperse moderately dense evaporating sprays, Commun. Comput. Phys. (2016) 1–41Accepted, available online at https://hal.archives-ouvertes.fr/hal-01169730.

[30] F. Doisneau, A. Sibra, J. Dupays, A. Murrone, F. Laurent, M. Massot, Numerical strategy for unsteady two-way coupling in polydisperse sprays: application to solid rocket motor instabilities, Journal of Propulsion and Power 30 (3) (2014) 727–748.

[31] J. A. Shohat, J. D. Tamarkin, The Problem of Moments, 4th Edition, American Mathematical Society, 1943.

[32] H. Dette, W. J. Studden, The Theory of Canonical Moments with Applications in Statistics, Probability, and Analysis, Wiley-Interscience, 1997.

[33] H. Dette, W. J. Studden, Matrix measures, moment spaces and Favard's theorem for the interval $[0, 1]$ and $[0, +\infty]$, Linear Algebra and its Applications 345 (2002) 169–193.

[34] M. Massot, F. Laurent, D. Kah, S. De Chaisemartin, A robust moment method for evaluation of the disappearance rate of evaporating sprays, SIAM Journal of Applied Mathematics 70 (2010) 3203–3234.

[35] M. Frenklach, S. J. Harris, Aerosol dynamics modeling using the method of moments, Journal of Colloid and Interface Science 118.

[36] M. Frenklach, Method of moments with interpolative closure, Chemical Engineering Science 57 (2002) 2229–2239.

[37] M. E. Mueller, G. Blanquart, H. Pitsch, A joint volume-surface model of soot aggregation with the method of moments, Proceedings of the Combustion Institute 32 (2009) 785–792.

[38] M. E. Mueller, G. Blanquart, H. Pitsch, Modeling the oxidation-induced fragmentation of soot aggregates in laminar flames, Proceedings of the Combustion Institute 33 (2011) 667–674.

[39] D. L. Marchisio, R. D. Vigil, R. O. Fox, Quadrature method of moments for aggregation–breakage processes, Journal of Colloid and Interface Science 258 (2) (2003) 322–334.

[40] R. McGraw, Description of aerosol dynamics by the quadrature method of moments, Aerosol Science and Technology 27 (1997) 255–265.

[41] D. L. Marchisio, R. O. Fox, Solution of population balance equations using the direct quadrature method of moments, Journal of Aerosol Science 36 (2005) 43–73.

[42] C. Yuan, R. O. Fox, Conditional quadrature method of moments for kinetic equations, Journal of Computational Physics 230 (2011) 8216–8246.

[43] R. O. Fox, F. Laurent, M. Massot, Numerical simulation of spray coalescence in an Eulerian framework: Direct quadrature method of moments and multi-fluid method, Journal of Computational Physics 227 (6) (2008) 3058–3088.

[44] A. Tagliani, Hausdorff moment problem and maximum entropy: a unified approach, Appl. Math. Comput. 105 (2-3) (1999) 291–305.

[45] L. R. Mead, N. Papanicolaou, Maximum entropy in the problem of moments, J. Math. Phys. 25 (8) (1984) 2404–2417.

[46] A. Vié, F. Laurent, M. Massot, Size-velocity correlations in hybrid high order moment/multifluid methods for polydisperse evaporating sprays: Modeling and numerical issues, Journal of Computational Physics 237 (2013) 177–210.

[47] D. Kah, F. Laurent, M. Massot, S. Jay, A high order moment method simulating evaporation and advection of a polydisperse liquid spray, Journal of Computational Physics 231 (2012) 394–422.

[48] A. Tagliani, Maximum entropy solutions and moment problem in unbounded domains, Appl. Math. Lett. 16 (4) (2003) 519–524.

[49] C. Yuan, F. Laurent, R. O. Fox, An extended quadrature method of moments for population balance equations, Journal of Aerosol Science 51 (2012) 1–23.

[50] G. A. Athanassoulis, P. N. Gavriliadis, The truncated Hausdorff moment problem solved by using kernel density functions, Probabilistic Engineering Mechanics 17 (3) (2002) 273–291.

[51] C. Chalons, R. O. Fox, M. Massot, A multi-Gaussian quadrature method of moments for gas-particle flows in a LES framework, in: Proceedings of the Summer Program 2010, Center for Turbulence Research, Stanford University, Stanford, 2010, pp. 347–358.

[52] E. Madadi-Kandjani, A. Passalacqua, An extended quadrature-based moment method with log-normal kernel density functions, Chemical Engineering Science 131 (2015) 323–339.

[53] S. Salenbauch, A. Cuoci, A. Frassoldati, C. Saggese, T. Faravelli, C. Hasse, Modeling soot formation in premixed flames using an extended conditional quadrature method of moments, Combustion and Flame 162 (6) (2015) 2529 – 2543.

[54] D. L. Wright, Numerical advection of moments of the particle size distribution in Eulerian models, Journal of Aerosol Science 38 (2007) 352–369.

[55] V. Vikas, Z. J. Wang, A. Passalacqua, R. O. Fox, Realizable high-order finite-volume schemes for quadrature-based moment methods, Journal of Computational Physics 230 (13) (2011) 5328–5352.

[56] V. Vikas, Z. J. Wang, R. O. Fox, Realizable high-order finite-volume schemes for quadrature-based moment methods applied to diffusion population balance equations, Journal of Computational Physics 249 (2013) 162–179.

[57] R. McGraw. Correcting moment sequences for errors associated with advective transport [online] (2006).

[58] A. Sibra, J. Dupays, A. Murrone, F. Laurent, M. Massot, Simulation of reactive polydisperse sprays strongly coupled to unsteady flows in solid rocket motors: Efficient strategy using eulerian multi-fluid methods, submitted, available online at https://hal.archives-ouvertes.fr/hal-01063816 (2015).

[59] F. Doisneau, F. Laurent, A. Murrone, J. Dupays, M. Massot, Eulerian multi-fluid models for the simulation of dynamics and coalescence of particles in solid propellant combustion, Journal of Computational Physics 234 (2013) 230–262.

[60] G. Blanquart, H. Pitsch, Analyzing the effects of temperature on soot formation with a joint volume-surface-hydrogen model, Combustion and Flame 156 (2009) 1614–1626.

[61] W. Gautschi, Orthogonal Polynomials: Computation and Approximation, Oxford University Press, 2004.

[62] T. S. Chihara, An Introduction to Orthogonal Polynomials, no. 13 in Mathematics and its Applications, Gordon and Breach Science Publishers, New York-London-Paris, 1978.

[63] H. Rutishauser, Der Quotienten-Differenzen-Algorithmus, Z. Angew. Math. Physik 5 (1954) 233–251.

[64] P. Henrici, The quotient-difference algorithm, Nat. Bur. Standards Appl. Math. Ser. (49) (1958) 23–46.

[65] R. G. Gordon, Error bounds in equilibrium statistical mechanics, Journal of Mathematical Physics 9 (5) (1968) 655–663.

[66] R. G. Gordon, Error bounds in spectroscopy and nonequilibrium statistical mechanics, Journal of Mathematical Physics 9 (7) (1968) 1087–1092.

[67] J. C. Wheeler, Modified moments and Gaussian quadratures, Rocky Mountain Journal of Mathematics 4 (1974) 287–296.

[68] W. H. Press, S. A. Teukolsky, W. T. Vetterling, B. P. Flannery, Numerical Recipes: The Art of Scientific Computing, 3rd Edition, Cambridge University Press, 2007.

[69] M. Wilck, A general approximation method for solving integrals containing a lognormal weighting function, Journal of Aerosol Science 32 (2001) 1111–1116.

[70] S. Gottlieb, D. Ketcheson, C.-W. Shu, Strong Stability Preserving Runge-Kutta and Multistep Time Discretizations, World Scientific, 2011.

[71] F. Gelbard, J. H. Seinfeld, Numerical solution of the dynamic equation for particulate systems, Journal of Computational Physics 28 (1978) 357–375.

[72] S. Vemury, S. E. Pratsinis, Self-preserving size distributions of agglomerates, Journal of Aerosol Science 26 (2) (1995) 175–185.

[73] G. Strang, On the construction and comparison of difference schemes, SIAM Journal of Numerical Analysis 5 (1968) 506–517.

[74] M. Mehta, V. Raman, R. O. Fox, On the role of gas-phase and surface chemistry in the production of titania nanoparticles in turbulent flames, Chemical Engineering Science 104 (2013) 1003–1018.

[75] A. Buffo, M. Vanni, D. L. Marchisio, R. O. Fox, Multivariate quadrature-based moment methods for turbulent polydisperse gas–liquid systems, International Journal of Multiphase Flow 50 (2013) 41–57.

[76] C. Yuan, B. Kong, A. Passalacqua, R. O. Fox, An extended quadrature-based mass-velocity moment model for polydisperse bubbly flows, The Canadian Journal of Chemical Engineering 92 (12) (2014) 2053–2066.

[77] J. C. Butcher, Numerical Methods for Ordinary Differential Equations, 2nd Edition, Wiley, 2008.

[78] E. Hairer, G. Wanner, Solving Ordinary Differential Equations I. Nonstiff Problems, 2nd Edition, Springer, 2009.

[79] E. Hairer, G. Wanner, Solving Ordinary Differential Equations II. Stiff and Differential-Algebraic Problems, 2nd Edition, Springer, 2010.